Carbonation behavior and mechanical performance of low-carbon recycled concrete under different CO_2 pressures

Hao Bao[a,b,c,*], Jie Wang[b], Gang Xu[a,b], Ruyu Wang[b], Mohamed Saafi[c], Jianqiao Ye[c,*]

a. Hubei Key Laboratory of Disaster Prevention and Mitigation, China Three Gorges University, Yichang, China

b. College of Civil Engineering & Architecture, China Three Gorges University, Yichang, China

c. Department of Engineering, Lancaster University, Lancaster LA1 4YR, UK

* Correspondence author: baohaowhu@163.com (H. Bao), j.ye2@lancaster.ac.uk (J. Ye).

Abstract: The construction industry faces challenges from high cement-related carbon emissions and construction waste. To address carbon reduction, sequestration, and waste utilization, accelerated carbonation tests were conducted on low-carbon recycled concrete (LCRC) to evaluate the effects of recycled aggregate (RA) replacement ratio of natural aggregate (NA), cement replacement ratio by ground granulated blast-furnace slag (GGBS), and external CO_2 pressure on carbonation depth and compressive strength. Microstructural analyses (SEM, EDX, MIP, and TGA-DSC) were conducted to analyze the microstructure, elemental distribution, pore structure, and compositional changes in LCRC before and after carbonation. Results showed that the LCRC carbonation depth increased and the compressive strength decreased with the increase of the RA and cement replacement ratios. The elevated external CO_2 pressure significantly accelerated carbonation, enhancing both carbonation depth and compressive strength. Under supercritical condition (7.5 MPa), the carbonation depth of the LCRC increased by an average of 164% compared to samples at 0.1 MPa, while the average compressive strength was 47% higher than that of the uncarbonated samples. Carbonation converts flocculent C-S-H gel into $CaCO_3$, refining the pore structure and reducing porosity by 28-34%. Based on the TGA result difference inversion, a method for determining $Ca(OH)_2$ and C-S-H contents in LCRC was proposed, revealing pre-carbonation contents of 17-37% and 63-83%, respectively. The maximum carbon uptake capacity reached 96.09 kg CO_2/m^3 of LCRC, highlighting its potential to support a low-carbon circular concrete industry.

Keywords: Low-carbon recycled concrete; Accelerated carbonation; Carbonation depth; Compressive strength; External CO_2 pressures.

1. Introduction

In recent years, the growing demand for concrete structural maintenance and construction has significantly boosted concrete usage, thereby accelerating the rise in global cement production. CO_2 emissions from cement production account for approximately 8% of global carbon emissions [1, 2]. To reduce the carbon footprint, partially replacing cement with mineral admixtures such as silica fume, fly ash, and GGBS not only improves concrete performance but also conserves energy and reduces emissions [3, 4]. Currently, the construction industry faces both the challenges of managing construction waste in landfills and the decline in NA resources [5, 6]. Recycling waste concrete into RA for new concrete production provides a practical solution to both challenges, yielding significant environmental and economic benefits [7, 8]. Furthermore, carbonation treatment of the concrete not only enhances its mechanical properties [9] but also

enables long-term CO_2 sequestration [10]. Therefore, carbonation treatment of LCRC at varying RA and cement replacement ratios can yield synergistic benefits, including reduced cement consumption, enhanced RA resource utilization, improved mechanical properties, and carbon sequestration.

Compared to the natural aggregate concrete (NAC), recycled aggregate concrete (RAC) shows characteristics like low-density, high-water absorption, and large porosity. By investigating the porosity characteristics at RA interface, Duan et al. [11] found that old mortar adhering to the surface of RA is the primary cause of high porosity in the interfacial transition zone (ITZ). Therefore, the partial replacement of NA with RA in concrete inevitably decreases its compressive strength [12], splitting tensile strength [13] and durability [14, 15]. However, this porous ITZ with interconnected pores also allow much higher CO_2 transport rates in RAC compared to in NAC [16, 17]. Carbonation treatment can densify RA and promote carbonation of new paste[18, 19], where $CaCO_3$ fills the pores and strengthens the microstructure, improving both the mechanical properties and durability of RAC while absorbing CO_2 [19, 20]. Silva et al. [21] found that the carbonation depth of RAC incorporating 100% RA was 2.15 times that of NAC. Satomi et al. [22] investigated the effect of RA replacement ratio on concrete mechanical properties, observing a 21% decrease in compressive strength for RAC incorporating 100% RA compared to NAC. Although compressive strength decreases with increasing RA replacement ratio, carbonation treatment can enhance the compressive strength of RAC [23, 24]. Therefore, studies on the carbonation and mechanical properties of LCRC under different RA replacement ratios are of great significance.

To mitigate the adverse effects of RAs on concrete mechanical properties, methods such as enhancing the bond strength of cement paste in porous concrete using nanomaterials [25] or optimizing the performance of ITZ [26] have been explored. However, employing nanomaterials to increase cement paste bond strength is costly, limiting its application. By incorporating mineral admixtures (silica fume, fly ash, and GGBS) or adjusting fine aggregate composition [27-30] expands the bonding area between cement paste and aggregate, fills internal voids, thereby enhancing concrete density [27]. This approach improves compressive strength [31] and durability [32] of RAC at the same time reducing cement usage [33]. Wang et al. [34] achieved an 8% increase in RAC compressive strength by adding 20% fly ash. Qureshi et al. [35] demonstrated that incorporating 30% GGBS refined RAC pore size and connectivity through the pozzolanic reaction-generated C-S-H gel, resulting in a 5-12% increase in compressive strength and a 13% reduction in water absorption. Furthermore, with carbonation treatment of concrete containing various mineral admixtures, the carbonation rates accelerate due to reduced alkali reserves, thereby increasing compressive strength [36, 37]. Although compressive strength decreases with increasing cement replacement ratios in RAC, carbonation can partially compensate the loss.

Accelerated carbonation not only absorbs CO_2 but also enhances compressive strength of RAC. Concrete carbonation involves accelerated carbonation treatment after concrete demolding, with its effectiveness influenced by carbonation temperature [38], humidity [39], duration [40], and CO_2 concentration [24]. The influence of CO_2 pressure on accelerated concrete carbonation has drawn significant attention. For instance, Xian et al. [41] conducted accelerated carbonation on ordinary concrete under atmospheric pressure and observed a 32% increase in early compressive strength compared to the uncarbonated specimens. Bao et

al. [42] studied steel fiber reinforced concrete subject to supercritical carbonation, achieving a maximum carbonation depth of 32.58 mm within 6 h. Pore volume decreased by up to 32.3% compared to pre-carbonation levels, while compressive strength increased by 25.1%-42.7% relative to the uncarbonated specimens. Existing studies have also explored accelerated carbonation of RAC or RA under varying pressure conditions. For example, Liu et al. [43] found that carbonating RAC incorporating 100% RA at 0.1 MPa (with CO_2 flow equivalent to 0.3% of cement mass) increased its 28 d compressive strength by 94% compared to uncarbonated specimens. Zhan et al. [44] conducted carbonation of RAC at 0.4 MPa, observing a 32% increase in early compressive strength. Ndiaye et al. [45] conducted accelerated carbonation experiments on RA at 2.0 MPa and 5.0 MPa. They observed that increasing CO_2 pressure enhanced its solubility in water, thereby accelerating the carbonation reaction rate. In summary, the carbonation of cementitious materials is markedly accelerated under elevated CO_2 pressure, leading to enhanced compressive strength and increased microstructural compactness. However, comprehensive macro- and micro-scale investigations on the carbonation behavior and compressive strength of LCRC under different external CO_2 pressures, from atmospheric to supercritical conditions remain limited.

The present study systematically investigates the effects of varying cement replacement ratios, RA replacement ratios, and external CO_2 pressures on the carbonation depth and compressive strength of LCRC. A series of microstructural characterization techniques-including scanning electron microscopy (SEM), energy-dispersive X-ray spectroscopy (EDX), mercury intrusion porosimetry (MIP), and thermogravimetric analysis (TGA-DSC) were employed to analyze the microstructure, elemental distribution, pore characteristics, and compositional evolution of LCRC during accelerated carbonation. The contents of C-S-H and $Ca(OH)_2$ before carbonation were quantified to assess the carbon sequestration potential of LCRC, thereby elucidating its carbonation mechanism under different external CO_2 pressures. It simultaneously demonstrates the dual potential of this approach to synergistically achieve resource recovery from construction waste and CO_2 sequestration.

2. Experimental investigation

2.1. Materials

2.1.1. Cement

Portland cement (P·O 42.5 N) from Anhui Shui'an Construction Group Co., Ltd was used. Its chemical composition is shown in Table 1, with a density of 2.97 g/cm^3.

Table 1 Chemical composition of cement (%).

Components	SiO_2	Fe_2O_3	Al_2O_3	CaO	K_2O	SO_3	Loss of ignition
By mass (%)	19.27	3.36	3.72	67.11	1.24	4.33	0.97

2.1.2. GGBS

The GGBS used in this study is grade S95, supplied by Anhui Shui'an Construction Group Co., Ltd. Its chemical composition is shown in Table 2. Its density is 2.84 g/cm^3, and the specific surface area is 424 m^2/kg.

Table 2 Chemical composition of GGBS (%).

Components	SiO_2	Al_2O_3	CaO	MgO	SO_3	Burn vectors
By mass (%)	33.06	15.04	39.29	9.96	1.9	0.75

2.1.3. Fine aggregates

The fine aggregate is sourced from natural river sand in the Yichang region. Its fineness modulus is 2.87, with a mud content of 2.7% and an apparent density of 2650 kg/m³. All parameters comply with relevant specifications. The particle size distribution of the river sands is shown in Table 3.

Table 3 Cumulative retained mass of river sands.

Particle size (mm)	4.75	2.36	1.18	0.60	0.30	0.15	<0.15
Cumulative retained mass (%)	0.39	17.65	38.76	60.88	79.79	91.86	99.95

2.1.4. Natural and recycled concrete aggregates

The NAs were sourced from local quarries in Yichang. The RAs were supplied by Yichang Environmental Protection Building Materials Co., Ltd., produced by crushing the construction waste first using a jaw crusher, and then purifying using air separation and magnetic separation. By mass, the RAs consisted of approximately 96% concrete aggregates and 4% brick aggregates. Before testing, both the NAs and the RAs were sieved by particle size using a vibrating sieve shaker equipped with wire mesh screens of 20 mm, 10 mm, and 5 mm apertures placed at the upper, middle, and lower layers, respectively. Aggregates with a particle size range of 5-20 mm were selected for the experiment, while impurities such as highly porous and low-density brick aggregates were removed. The particle size distributions of (5-20 mm) were determined according to GB/T 14685-2022 [46]. The results are summarized in Table 4. To ensure adequate workability of the RAC and mitigate the adverse effects of the high water absorption of the RA on the concrete mix proportion, all the RAs were pre-treated to a saturated surface-dry (SSD) condition [47]. Specifically, the RA was immersed in a water tank for 24 h to achieve a uniform and stable moisture content [48]. The aggregate surface was then wiped with a dry cloth until no visible water film remained, achieving the saturated surface dry state [49].

Table 4 Cumulative screen residue of RA.

Particle size (mm)	20	16	10	5
Cumulative screen residue by mass (%)	0.00	21.6	52.9	96.15

The physical properties of the NA and RA were tested according to GB/T 14685-2022 [46] and GB/T 25177-2010 [50], respectively. For the crushing test, 3000 g of 9.5-19 mm aggregate was subjected to 200 kN pressure loading. The pass rate through a 2.36 mm sieve opening was calculated. The specific test results are summarized in Table 5. The results indicate that the crushing value of the RA meets the specification requirements.

Table 5 Physical properties of coarse aggregates.

Coarse aggregates type	Apparent density (kg/m^3)	Water absorption (%)	Crush value (%)
NAs	2820	3.8	7.27
RAs	1974	18.7	29.3

2.2. Mix proportion and preparation

To investigate the influence of RA replacement ratios, cement replacement ratios, and external CO_2 pressure on the carbonation depth and compressive strength of LCRC, cement replacement ratios of 0%, 10%, 20%, and 30%, and RA replacement ratios of 0%, 50%, and 100% were adopted. The external CO_2 pressure

was controlled at 0.1, 1.0, 3.0, 5.0, and 7.5 MPa. In this study, NA was replaced by RA on a mass basis, resulting in an increased aggregate volume fraction due to the lower density of RA. This volumetric effect was regarded as an inherent feature of RA incorporation and was retained to reflect practical engineering conditions. The mix proportions of the LCRC are shown in Table 6, with a total of 12 mix designs. To reduce the effect of material heterogeneity on the carbonation results, for each mix design, 3 specimens were used to measure the average compressive strength after carbonation, and 3 specimens for the carbonation depth. Considering five levels of external CO_2 pressure for each mix, a total of 30 specimens were tested. In addition, for each mix design, 3 specimens were selected for compressive strength testing before carbonation, and 3 specimens were used for drying curve measurements of uncarbonated specimens. Therefore, 36 specimens were cast for each mix design, resulting in a total of 432 specimens.

Due to the limited internal space of the reaction chamber, coupled with the installation of a temperature probe at the center of the chamber lid, which incorporates a vertical sensor extending to the bottom for continuous monitoring of the temperature inside the chamber, the LCRC specimens were fabricated as cubes with a side length of 70.7 mm. This dimension allows the chamber to accommodate up to nine specimens without obstructing the temperature probe. The same dimension of the concrete cubes were also used in prior investigations to quantify carbonation depth [51, 52] and to evaluate compressive strength before and after carbonation [53, 54].

Before casting the LCRC specimens, the inner surfaces of the molds were uniformly coated with LF-50305 water-based release agent. This milky-white emulsion, manufactured by Wenzhou Nuofu Building Materials Co., Ltd., requires about 30 min to form a stable film. Its primary constituents include sodium dodecyl benzenesulfonate, among others. The concrete was cast using the mix proportions presented in Table 5. The slump of the fresh concrete was measured according to GB/T 50080-2016 [55] by filling the mold in layers (25 tamping strokes per layer), vertically removing it, and measuring the height difference between the mold and the slumped specimens. The specimens were demolded after 24 h. During the curing period, cementitious materials undergo hydration, and their internal pores are typically filled with a saturated $Ca(OH)_2$ solution [56]. To ensure an initial pore water saturation of 100% and maintain a relative humidity of no less than 95% during subsequent curing, this measure prevents leaching of Ca^{2+} from the cementitious matrix and facilitates continuous hydration of the cement in a high-humidity environment. The demolded specimens were immersed in a 0.0118 mol/L saturated $Ca(OH)_2$ solution and cured at (20±2) °C for 28 d. This procedure ensured control over the initial pore water saturation of the specimens.

Table 6 Mix proportions and 28 d compressive strength of LCRC cured in saturated $Ca(OH)_2$ solution.

Groups	W/C	Cement (kg/m^3)	GGBS (kg/m^3)	Fine aggregates (kg/m^3)	Coarse aggregates		Water (kg/m^3)	Water reducing agent (kg/m^3)	Slump values (mm)
					Natural (kg/m^3)	Recycled (kg/m^3)			
C-CR0%-CA0%	0.49	411.00	0.00	750.00	1037.00	0.00	201.00	10.30	155
C-CR10%-CA0%	0.49	369.90	41.10	750.00	1037.00	0.00	201.00	10.30	160
C-CR20%-CA0%	0.49	328.80	82.20	750.00	1037.00	0.00	201.00	10.29	160
C-CR30%-CA0%	0.49	287.70	123.30	750.00	1037.00	0.00	201.00	10.29	170
C-CR0%-CA50%	0.49	411.00	0.00	750.00	518.50	518.50	201.00	10.29	160
C-CR10%-CA50%	0.49	369.90	41.10	750.00	518.50	518.50	201.00	10.29	170

Groups	W/C	Cement (kg/m^3)	GGBS (kg/m^3)	Fine aggregates (kg/m^3)	Coarse aggregates		Water (kg/m^3)	Water reducing agent (kg/m^3)	Slump values (mm)
					Natural (kg/m^3)	Recycled (kg/m^3)			
C-CR20%-CA50%	0.49	328.80	82.20	750.00	518.50	518.50	201.00	10.29	165
C-CR30%-CA50%	0.49	287.70	123.3	750.00	518.50	518.50	201.00	10.29	175
C-CR0%-CA100%	0.49	411.00	0.00	750.00	0.00	1037.00	201.00	10.29	170
C-CR10%-CA100%	0.49	369.90	41.10	750.00	0.00	1037.00	201.00	10.29	165
C-CR20%-CA100%	0.49	328.80	82.20	750.00	0.00	1037.00	201.00	10.29	175
C-CR30%-CA100%	0.49	287.70	123.30	750.00	0.00	1037.00	201.00	10.29	185

Remarks: C-CR10%-CA50% denotes the LCRC specimens with a cement replacement ratio of 10% and RA replacement ratio of 50%.

2.3. *Regulation of pore water saturation*

As a heterogeneous material, a cement-based material exhibits non-uniform pore water distribution [57], which influences its carbonation process [58] and consequently alters the carbonation outcomes. Numerous studies have demonstrated that when the pore water saturation is 0.50 [58, 59], concrete exhibits an increased carbonation rate, a more rapid carbonation process, and a greater carbonation depth. To precisely adjust the pore water saturation to 0.50, the specimens were removed after curing, and their pore water saturation was regulated accordingly. The detailed procedure is described as follows.

(1) Three specimens were randomly selected from each mix ratio group listed in Table 5, yielding a total of 36 specimens. After the removal of surface moisture, the saturated mass of each specimen was measured using an electronic balance (Model FD-C60002, Kunshan U-Kovet Electronics Technology Co., Ltd., China). The average mass for each group, denoted as m_s, was then calculated.

(2) The specimens were oven-dried at 60°C. During this process, they were weighed every 8 h for the first 24 h and then every 24 h thereafter, with the average mass of each group recorded as m_i. This drying and weighing cycle was repeated until the mass loss between two successive measurements was less than 0.2 g, at which point the specimens were considered to have reached a completely dry state. The corresponding average mass of each group was denoted as m_0.

(3) From Eq. (1), the pore water saturation of the specimens at each drying interval was calculated and denoted as S_i.

$$S_i = \frac{m_i - m_0}{m_s - m_0} \tag{1}$$

where i denotes the drying time (h), m_i represents the mass of the specimen at each drying interval (g), m_0 denotes the mass of the specimen after reaching a constant dry state (g), and m_s denotes the mass of the specimen in a fully saturated state (g).

The method used to control the pore water saturation of the specimens is illustrated in Fig. 1.

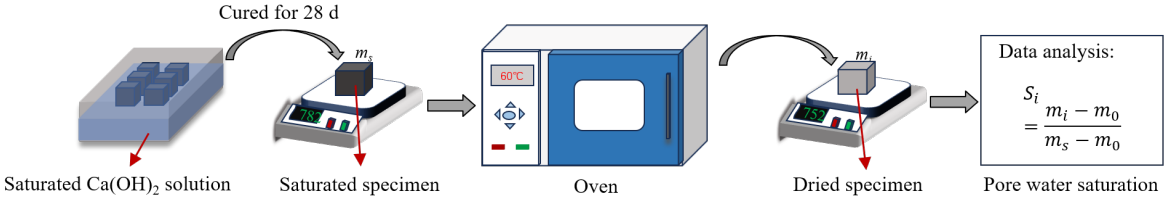

Fig. 1. Procedure for controlling pore water saturation of specimens.

The pore water saturation of specimens at each drying interval was calculated using the above-mentioned method, and the variation of water saturation against drying time were approximately plotted. It was found that the overall trend of the pore water saturation for specimens of different mix ratios was essentially similar. Without loss of generality, the groups with 0% cement replacement and with RA replacement ratios of 0%, 50%, and 100% were selected as the representative group. The variation of pore water saturation with drying time for the representative group is shown in Fig. 2. Based on curve fitting, a mathematical relationship was established and subsequently employed to calculate the time required for the pore water saturation of the LCRC specimens to reach 0.5.

Based on the fitting formula of the drying curve in Fig. 2, determine the drying time for specimens and dry them according to their respective drying times. After adjusting the pore water saturation to 0.5, all specimens were pretreated for 30 days in a YH-90B constant temperature/humidity chamber (20±2°C, 50% relative humidity) to achieve uniform distribution of pore water saturation throughout the specimens [60].

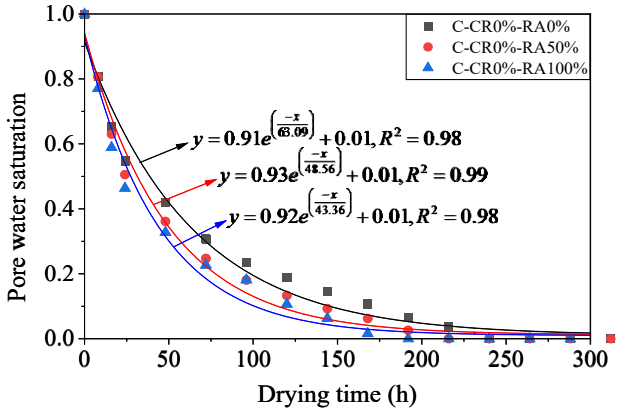

Fig. 2. Drying curves of LCRC with 0% cement replacement and RA replacement ratios of 0%, 50%, and 100% at 60°C.

2.4. Accelerated carbonation test of LCRC

To investigate the effects of varying RA and cement replacement ratio on the carbonation depth and mechanical properties of LCRC under different external CO_2 pressures, a supercritical carbonation apparatus for LCRC was assembled, as shown by the schematic pressurized carbonation system in Fig. 3. The reaction chamber (Model SLD20, Beijing Century Langsen Laboratory Instruments Co., Ltd., China) was designed for a maximum temperature of 200 °C and a maximum pressure of 12.5 MPa. The CO_2 pressurization system comprises a gas booster pump (Model DGS-DGA25-H, Dongguan Saicente Fluid Control Equipment Co., Ltd., China), assisted by an air compressor (Model HR230331A, Taizhou Pufeng Electromechanical Co., Ltd., China) and a filter (Model 015QPS). The gas booster pump operates within a driving pressure range of 2-8 bars, while the air compressor functions at 0.8 MPa. The CO_2 employed in this experiment was supplied by Yichang Dexin Practical Gas Co., Ltd., with a purity of $\geqslant$99.5%. The detailed procedures for the accelerated carbonation test are described as follows.

(1) After reaching the target pore water saturation, the specimens were arranged on the material rack within the reaction chamber. Three specimens were positioned on each layer of the rack, resulting in a total of three layers. Once all specimens were positioned, the chamber cover was closed and fastened by tightening the high-strength bolts connecting the cover to the chamber body with a torque wrench.

(2) The inlet valve of the reaction chamber was closed, and the outlet valve was opened to connect the chamber to a vacuum pump (Model OLF750AFV, Shanghai Jaguar Compressor Manufacturing Co., Ltd., China). The vacuum pump was then activated until a vacuum of 101.325 kPa was achieved inside the chamber, at which point the outlet valve was closed and the pump was simultaneously turned off.

(3) The high-pressure valve of the booster pump was opened while the unloading valve was closed. The CO_2 cylinder valve and the reaction chamber inlet valve were then opened to inject CO_2 into the chamber. Once the target pressure was reached, both valves were immediately closed. To achieve a pressure above 5.0 MPa, the air compressor was started first, followed by opening the drive gas valve on the booster pump. The drive gas compressed the CO_2 via the drive piston before injection into the reaction chamber. Upon reaching the preset pressure, the inlet valve, drive gas valve, and CO_2 cylinder valve were closed sequentially.

(4) The target CO_2 pressures within the reaction chamber were set at 0.1, 1.0, 3.0, 5.0, and 7.5 MPa. At each of the target pressures, during the pressurization and carbonation stages, the specimens were maintained at the designed pressure for 6 h, with the temperature and pressure in the reaction chamber being recorded at 10 min intervals. The temperature and pressure curves for representative specimens during the carbonation are shown in Fig. 4.

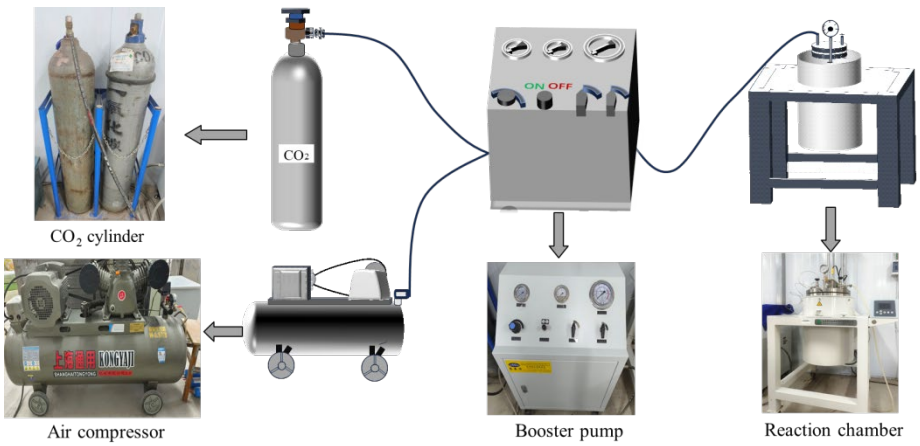

Fig. 3. Schematic diagram of the accelerated carbonation system.

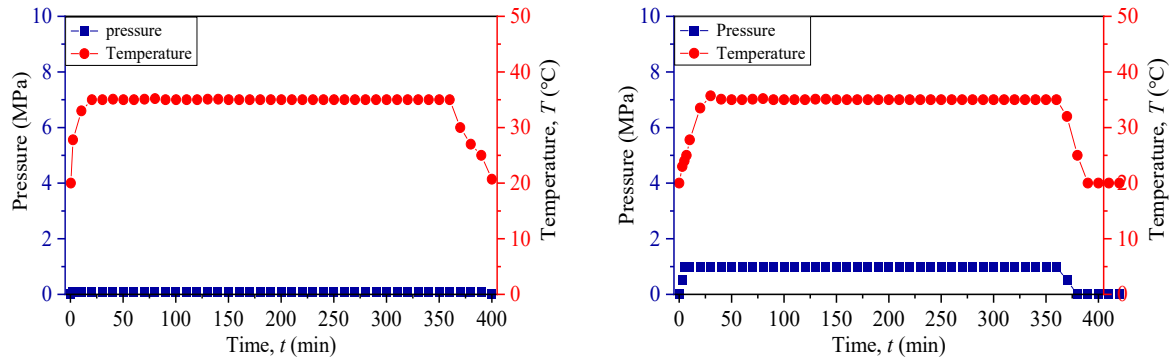

(a) 0.1 MPa (b) 1.0 MPa

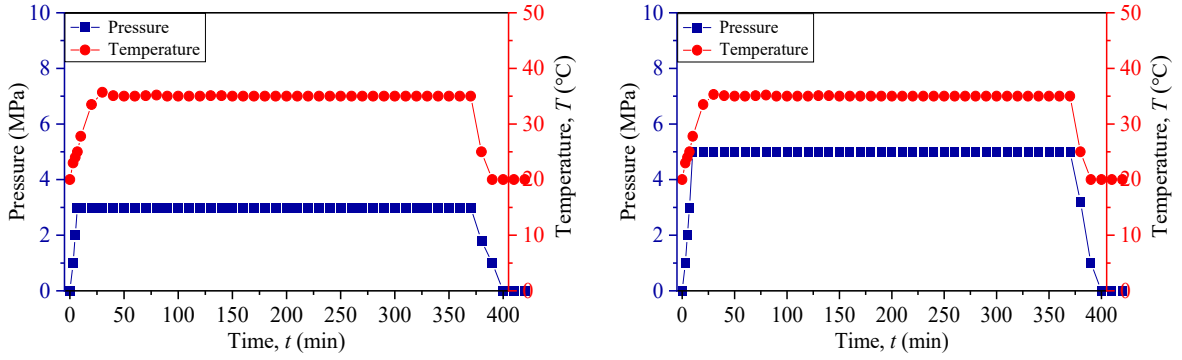

(c) 3.0 MPa (d) 5.0 MPa

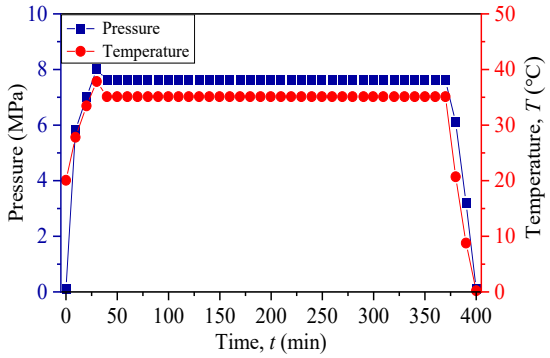

(e) 7.5 MPa

Fig. 4. Temperature and pressure variations of C-CR0%-RA0% specimens over time.

2.5. Carbonation depth measurement of LCRC

The specimens were taken out and tested for carbonation depth after carbonation reaction. Fig. 5 shows the testing process. Each sample was first cut in half using a cutting machine, and any residual powder was removed with a rubber air blower. The carbonation depth was then measured using the phenolphthalein alcohol indicator method. In accordance with the carbonation test method specified in the standard GB/T 50082-2024 [61], a 1% phenolphthalein solution was prepared and sprayed onto the concrete surface. The uncarbonated areas turned purple, while the fully carbonated regions remained colorless. Measurements were taken at 10 mm intervals along the surface using a vernier caliper. The carbonation depth was calculated using Eq. (2).

$$d = \frac{1}{n}\sum_{i=1}^{n} d_i \tag{2}$$

where d is the average carbonation depth at a curing age of 28 d (mm); d_i is the carbonation depth at each measurement point (mm); and n is the number of measurement points.

2.6. Compressive strength test of LCRC

After the carbonation test, some of the specimens were taken out for compressive strength testing, which was conducted in accordance with GB/T 50081-2019 [62]. The tests were performed using a microcomputer-controlled electro-hydraulic servo universal testing machine (Model WAW-2000, Shanghai Sansi Zongheng Machinery Manufacturing Co., Ltd., China) with a maximum load capacity of 2000 kN, applying the load at a rate of 3 kN/s. The compressive strength was calculated by Eq. (3), while the loads (including the ultimate

load) and the corresponding displacements were automatically recorded by the microcomputer system during loading. The compressive strength testing procedure is illustrated in Fig. 5.

$$f_c = \frac{F_{\max}}{A} \tag{3}$$

In Eq. (3), f_c is the compressive strength of the specimen (MPa), F_{max} is the failure load (N), and A is the bearing area of the specimen (mm^2). For each group, the compressive strength was taken as the arithmetic mean of the three measured specimens, with an accuracy of 0.1 MPa.

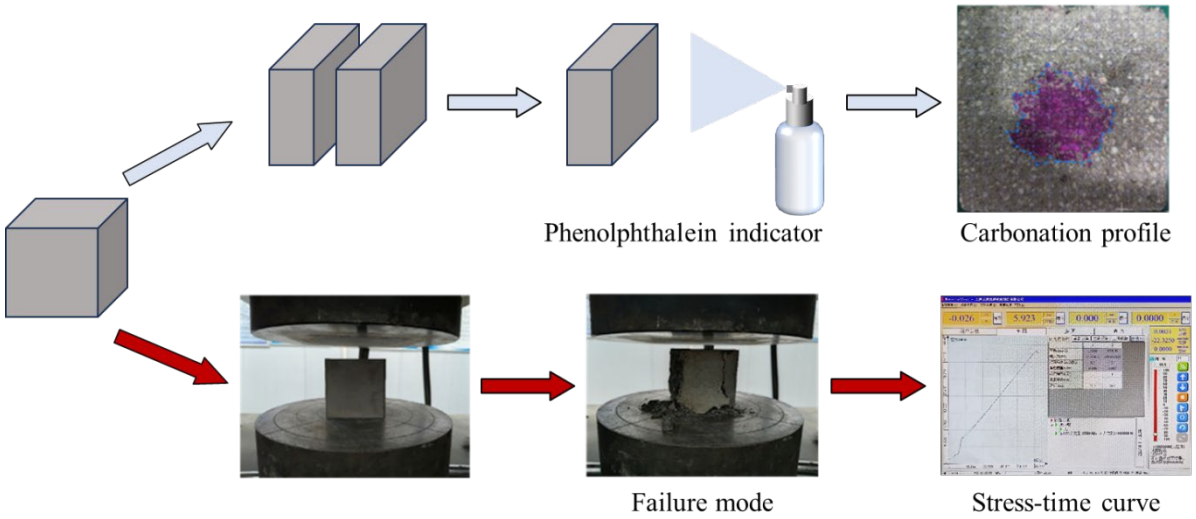

Fig. 5. Schematic diagram of carbonation depth and compressive strength test of LCRC.

2.7. Characterization of microstructural and compositional evolution

2.7.1. SEM observations

To investigate the microstructural characteristics of the LCRC before and after carbonation, both uncarbonated and carbonated samples were ground, and particles measuring 2-3 mm were selected. Following cleaning, the samples were oven-dried at 60°C for 24 h. A thin gold (Au) coating was then applied using a JFC-1600 sputtering coater. The crystalline morphology and pore structure of the samples, before and after carbonation under different CO_2 pressures, were examined using a SEM (Model JSM-7500F, JEOL Ltd., Japan) operated at an accelerating voltage of 20 kV and a magnification of 20000×. Furthermore, elemental composition analysis was performed using a X-ray fluorescence analyzer (Model EDX-7000, Shimadzu Corporation, Japan).

2.7.2. MIP measurement

To evaluate the effects of supercritical carbonation on the pore structure of concrete with different cement replacement ratios, samples were collected from both the carbonated and uncarbonated zones and subsequently pulverized. Particles with sizes ranging from 3 to 5 mm were selected and immersed in anhydrous ethanol for 48 h to terminate hydration. The samples were then dried at 85°C, cooled to room temperature, and sealed to prevent further carbonation. The pore structure of the prepared specimens was characterized using a porosimeter (Model AutoPore IV 9500, Mc Instruments, Inc., USA). In this study, porosity refers to the total intrusion porosity obtained from MIP measurements. It is defined as the cumulative

volume of mercury intruded at the maximum applied pressure, expressed as a percentage of the specimen's bulk volume. The measurement covers a pore diameter range from approximately 357 μm down to 3 nm.

2.7.3. TGA-DSC measurement

To investigate the variations in $CaCO_3$ and $Ca(OH)_2$ contents in the carbonated and uncarbonated zones of the LCRC under different CO_2 pressures, samples from the two zones were crushed and ground into powder. TGA-DSC was performed using a simultaneous thermal analyzer (Model STA449F5, Netzsch, Germany). Prior to the testing, the samples were oven-dried at 40°C for 24 h, ground into powder, and sieved through an 80 μm mesh. During the test, nitrogen was used as purge gas, and the specimens were heated to 1000°C at a constant heating rate of 10°C/min, while the mass change of the samples was continuously monitored.

2.8. Quantification of C-S-H and $Ca(OH)_2$ contents from TGA-DSC results

This study employs an analytical method using supercritical carbonation to quantitatively determine the $Ca(OH)_2$ and C-S-H contents in concrete prior to carbonation. The method calculates the mass of generated $CaCO_3$ and the residual $Ca(OH)_2$ mass from the thermogravimetric analysis of fully carbonated specimens. Combined with the initial $Ca(OH)_2$ content in the uncarbonated specimens, this determines the mass of $Ca(OH)_2$ participating in the reaction. In ordinary Portland cement, other hydration products (such as calcium aluminate hydrates) are present in low concentrations, and the carbonation of un-hydrated components is negligible [63]. Therefore, it can be assumed that the carbonation reaction originates solely from the participation of $Ca(OH)_2$ and C-S-H. Based on this assumption, the C-S-H content involved in the carbonation reaction can be further calculated by combining the total $CaCO_3$ formation with the mass of $Ca(OH)_2$ participating in the reaction. The specific calculation formula is as follows [60]:

$$m_{CC} = \left(D_{800} - D_{600}\right) \times m \tag{4}$$

$$m_{CH} = \left(D_{550} - D_{400}\right) \times m \tag{5}$$

$$m_{CH \to CC} = \frac{m_{CH}}{M_{\mathrm{CH}}} \times M_{\mathrm{CC}} \tag{6}$$

$$m_{C-S-H} = \frac{m_{CC} - m_{CH \to CC}}{3M_{\mathrm{CC}}} M_{\mathrm{C\text{-}S\text{-}H}} \tag{7}$$

$$P_{CH} = \frac{m_{CH}}{m_{CH} + m_{C-S-H}} \tag{8}$$

$$P_{C-S-H} = 1 - P_{CH} \tag{9}$$

where D_{800} represents the mass loss at 800°C, determined by the TGA-DSC test. m is the mass of the powder sample used in the TGA-DSC test. m_{CC} refers to the total mass of $CaCO_3$ produced by the carbonation reaction, while m_{CH} denotes the mass of $Ca(OH)_2$ involved in the carbonation reaction. $m_{CH \to CC}$ represents the mass of $CaCO_3$ derived from $Ca(OH)_2$. The molar mass of $Ca(OH)_2$ (M_{CH}) is 74 g/mol, and the molar mass of $CaCO_3$ (M_{CC}) is 100 g/mol. Additionally, $m_{C\text{-}S\text{-}H}$ signifies the mass of C-S-H involved in the carbonation reaction, with its molar mass ($M_{C\text{-}S\text{-}H}$) being 342 g/mol. The percentage content of $Ca(OH)_2$ and

C-S-H are denoted as P_{CH} and $P_{C\text{-}S\text{-}H}$, respectively.

3. Results and discussion

3.1. Pattern of LCRC carbonation depth variation

3.1.1. Effect of RA replacement ratio

To evaluate the effect of RA replacement ratio on the carbonation depth of LCRC, specimens were selected with RA replacement ratios of 0%, 50%, and 100%, and cement replacement ratios of 0%, 10%, 20%, and 30%. Following the procedure described in Section 2.3, the pore water saturation of these specimens was adjusted to 0.50. Accelerated carbonation tests were then conducted under different pressures according to the method outlined in Section 2.4. The carbonation depth was measured based on the approach specified in Section 2.5. Without loss of generality, the results for the 20% cement replacement LCRC are presented in Fig. 6. After spraying with phenolphthalein solution, the concrete surface showed distinct zones: the colorless carbonated areas and the dark purple-red uncarbonated areas. The carbonation depth of all experimental groups was calculated using Eq. (2), and the processed results are shown in Fig. 7.

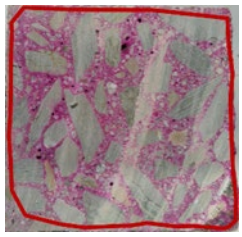

(a) C-CR20%-RA0%-0.1MPa

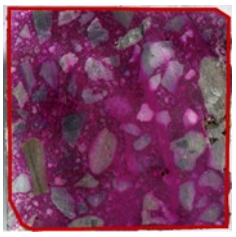

(b) C-CR20%-RA50%-0.1MPa

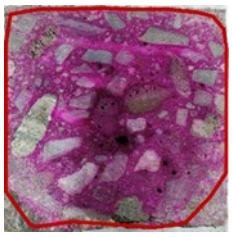

(c) C-CR20%-RA100%-0.1MPa

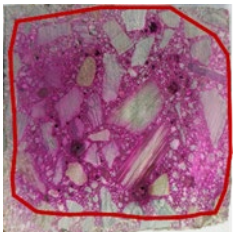

(d) C-CR20%-RA0%-1MPa

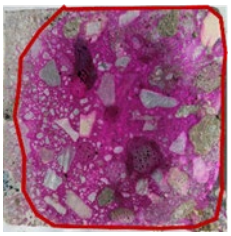

(e) C-CR20%-RA50%-1MPa

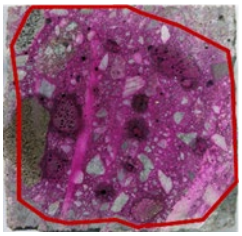

(f) C-CR20%-RA100%-1MPa

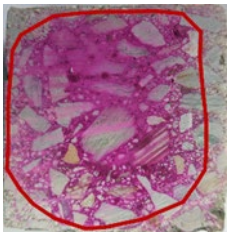

(g) C-CR20%-RA0%-3MPa

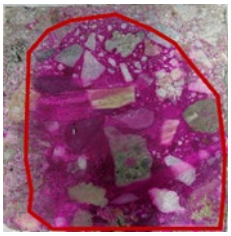

(h) C-CR20%-RA50%-3MPa

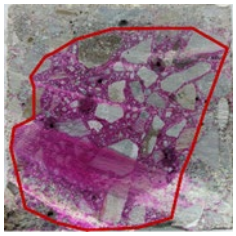

(i) C-CR20%-RA100%-3MPa

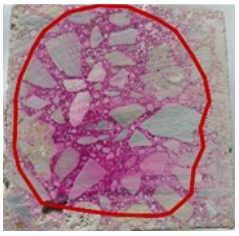

(j) C-CR20%-RA0%-5MPa

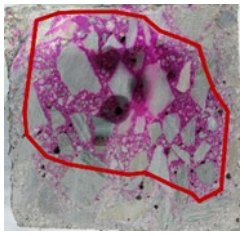

(k) C-CR20%-RA50%-5MPa

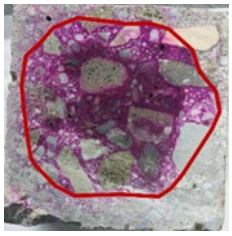

(l) C-CR20%-RA100%-5MPa

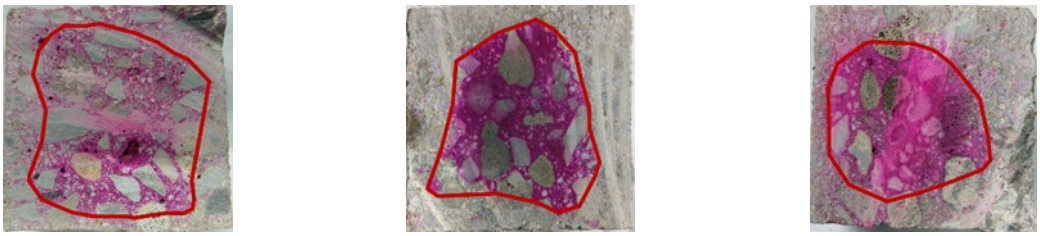

(m) C-CR20%-RA0%-7.5MPa (n) C-CR20%-RA50%-7.5MPa (o) C-CR20%-RA100%-7.5MPa

Fig. 6. Carbonation morphology of LCRC under different RA replacement ratios.

As shown in Fig. 6, under the identical external CO_2 pressure and cement replacement ratio, the colorless carbonated area indicated by the phenolphthalein solution significantly expanded as the RA replacement ratio increased from 0% to 100%, indicating a clear increase in carbonation depth. Under different RA replacement ratios, shown in Fig. 7, the carbonation depth exhibited an increasing trend with higher RA content across all external CO_2 pressure levels.

At an external CO_2 pressure of 0.1 MPa (Fig. 7a), the carbonation depth gradually increased with a 50% RA replacement ratio but rose significantly when the replacement ratio reached 100%. Further analysis of the test results under different pressure conditions (Figs. 7b-e) revealed that, at identical external CO_2 pressure and cement replacement ratio, the average carbonation depth of the LCRC with 50% and 100% RA replacement ratios increased by 13% and 26%, respectively, compared to the LCRC with a RA replacement ratio of 0%. This can be attributed to the higher water absorption (18.7%) and lower apparent density (1974 kg/m^3) of the RA (as listed in Table 4), which confirms the higher internal porosity of RAC. This porous nature provides additional diffusion pathways for CO_2, thereby accelerating carbonation. These results are consistent with the previously emphasized conclusion that RA porosity accelerates carbonation [21, 64], confirmed that even in LCRC with GGBS admixture, the permeability of RA remains the dominant factor promoting deeper CO_2 penetration.

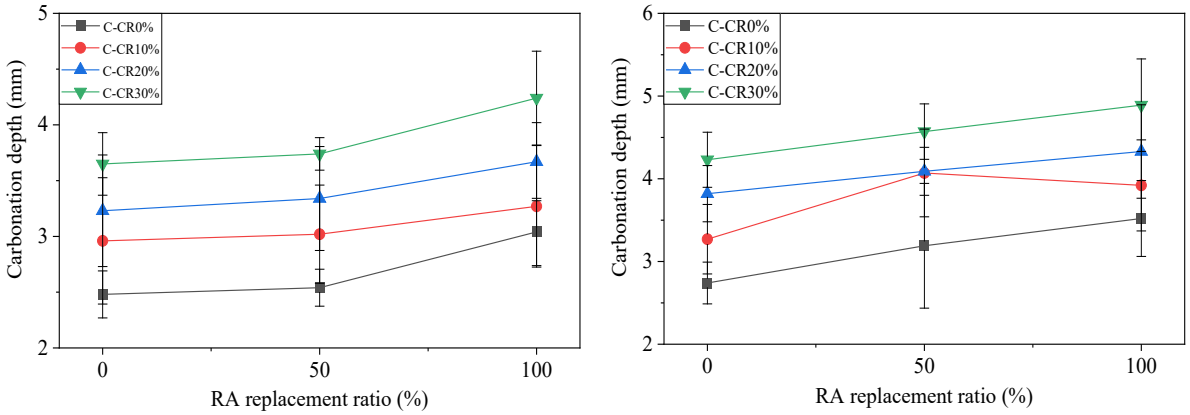

(a) 0.1 MPa (b) 1.0 MPa

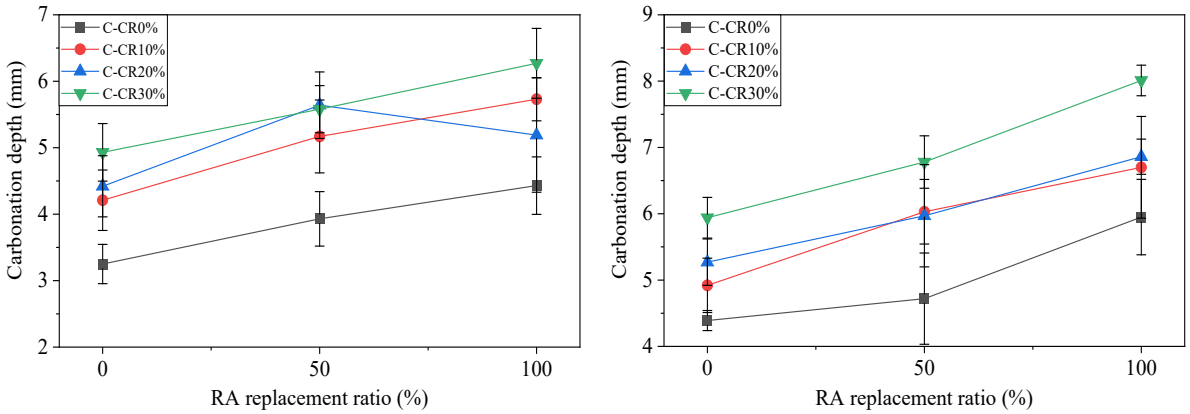

(c) 3.0 MPa (d) 5.0 MPa

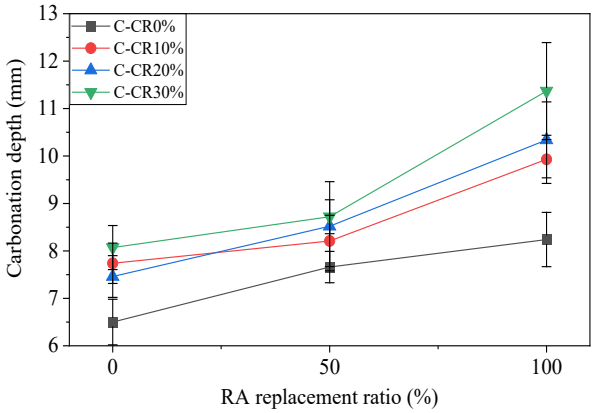

(e) 7.5 MPa

Fig. 7. Carbonation depth of LCRC with different RA replacement ratios.

3.1.2. Effect of cement replacement ratio

To investigate the effect of different cement replacement ratios on the carbonation depth of LCRC, specimens with a constant RA replacement ratio of 0%, 50%, and 100%, and cement replacement ratios of 0%, 10%, 20%, and 30% were subjected to carbonation under various CO_2 pressures. Without loss of generality, the carbonation profiles of 50% RA replacement LCRC are shown in Fig. 8, and the calculated carbonation depths for all experimental groups are summarized in Fig. 9.

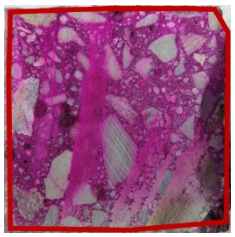

(a) C-CR0%-RA50%-0.1MPa

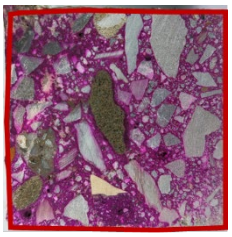

(b) C-CR10%-RA50%-0.1MPa

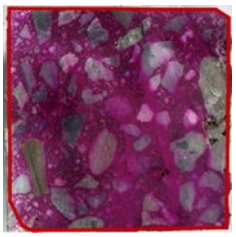

(c) C-CR20%-RA50%-0.1MPa

(d) C-CR30%-RA50%-0.1MPa

(e) C-CR0%-RA50%-1MPa

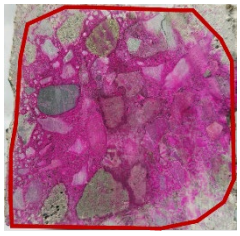

(f) C-CR10%-RA50%-1MPa

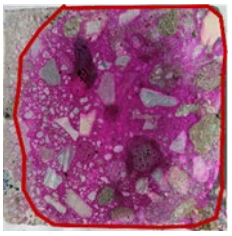

(g) C-CR20%-RA50%-1MPa

(h) C-CR30%-RA50%-1MPa

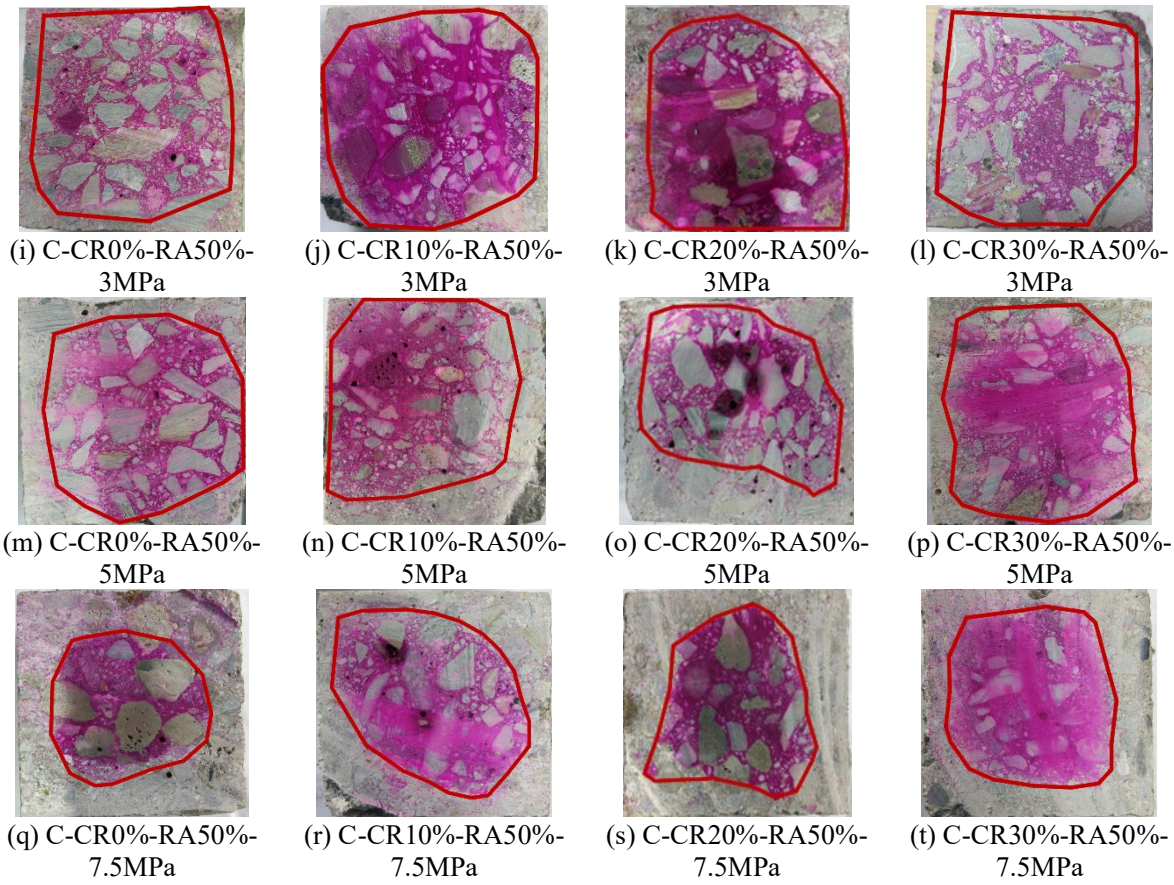

(i) C-CR0%-RA50%-3MPa (j) C-CR10%-RA50%-3MPa (k) C-CR20%-RA50%-3MPa (l) C-CR30%-RA50%-3MPa

(m) C-CR0%-RA50%-5MPa (n) C-CR10%-RA50%-5MPa (o) C-CR20%-RA50%-5MPa (p) C-CR30%-RA50%-5MPa

(q) C-CR0%-RA50%-7.5MPa (r) C-CR10%-RA50%-7.5MPa (s) C-CR20%-RA50%-7.5MPa (t) C-CR30%-RA50%-7.5MPa

Fig. 8. Carbonation morphology of LCRC under different cement replacement ratios.

Fig. 8 illustrates the influence of the cement replacement ratio on the carbonation morphology of the specimens. As the replacement ratio increases from 0% to 30%, the colorless carbonated region on the cross-section gradually expands, indicating a progressive increase in carbonation depth. In particular, under external CO_2 pressure of 5.0 MPa and 7.5 MPa (Figs. 8m-t), the carbonation front of the concrete with 30% cement replacement is noticeably deeper and exhibits a more distinct and well-defined boundary compared with the control mix. As shown in Figs. 9(a)-(e), under identical external CO_2 pressure and RA replacement ratio, the carbonation depth of LCRC exhibits an increasing trend with rising cement replacement ratios. The carbonation depth of LCRC with 10%, 20%, and 30% cement replacement ratios increased by 20%, 26%, and 40% on average, respectively, compared to the LCRC with 0% cement replacement. This is attributed to the increased cement replacement ratio, reducing cement content, thereby diluting and consuming the $Ca(OH)_2$ produced during hydration. This leads to a decrease in the alkaline reserve within the LCRC, resulting in increased carbonation depth of LCRC [65]. TGA-DSC test results (Fig. 18) confirm that higher cement replacement ratios reduce the calcium source available for carbonation reactions, allowing CO_2 to penetrate more easily into deeper regions. This indicates that when designing LCRC, a balance must be sought between reducing cement content and maintaining sufficient durability.

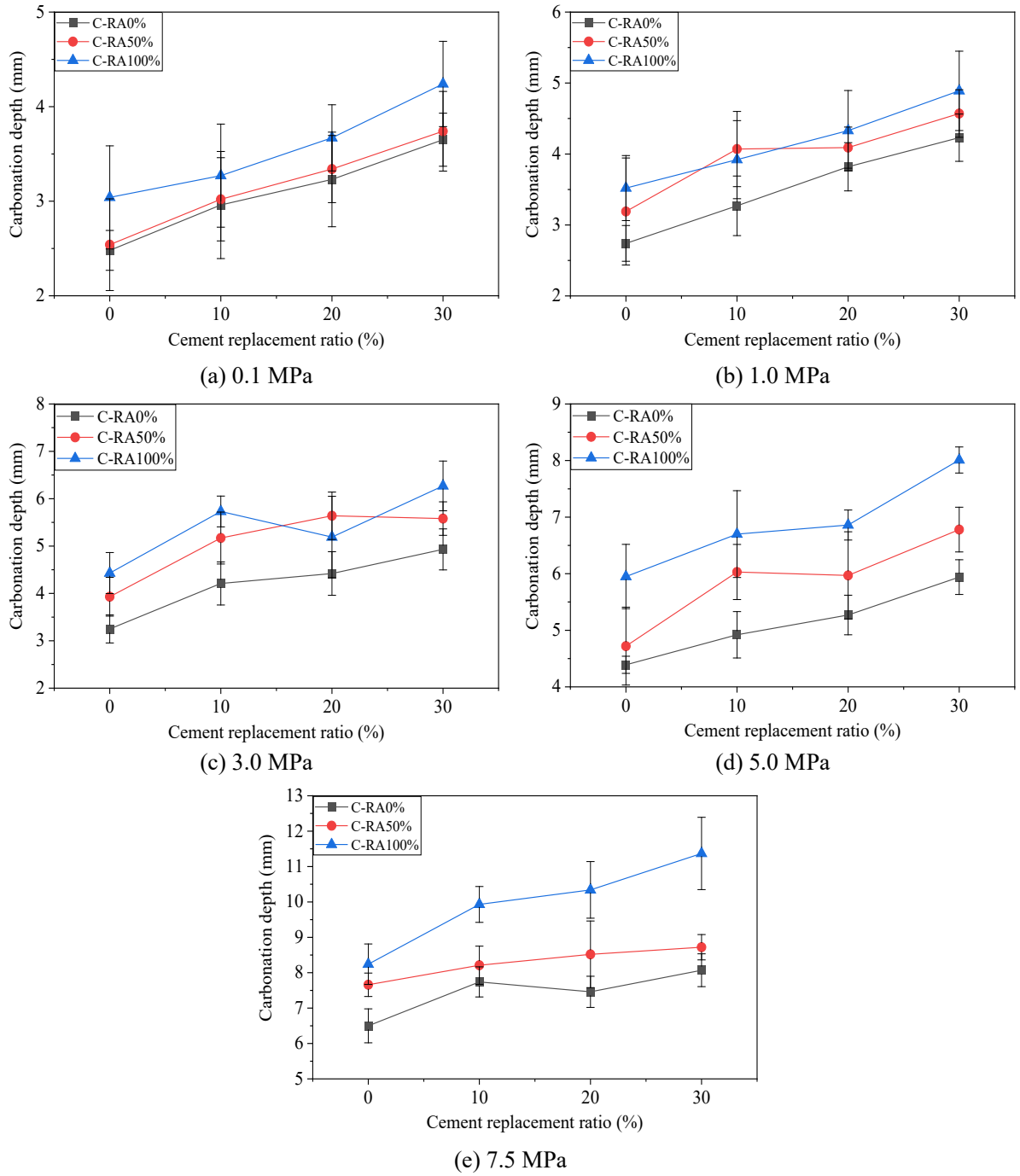

Fig. 9. Carbonation depth of LCRC with different cement replacement ratios.

3.1.3. Effect of external CO_2 pressure

Without loss of generality, Fig. 10 partly shows the carbonation morphology of the LCRC under external CO_2 pressures of 0.1 MPa, 1.0 MPa, 3.0 MPa, 5.0 MPa, and 7.5 MPa, with RA replacement ratios of 0%, 50%, and 100% and a fixed cement replacement ratio of 20%. The carbonation depth measurements across all experimental groups are presented in Fig. 11.

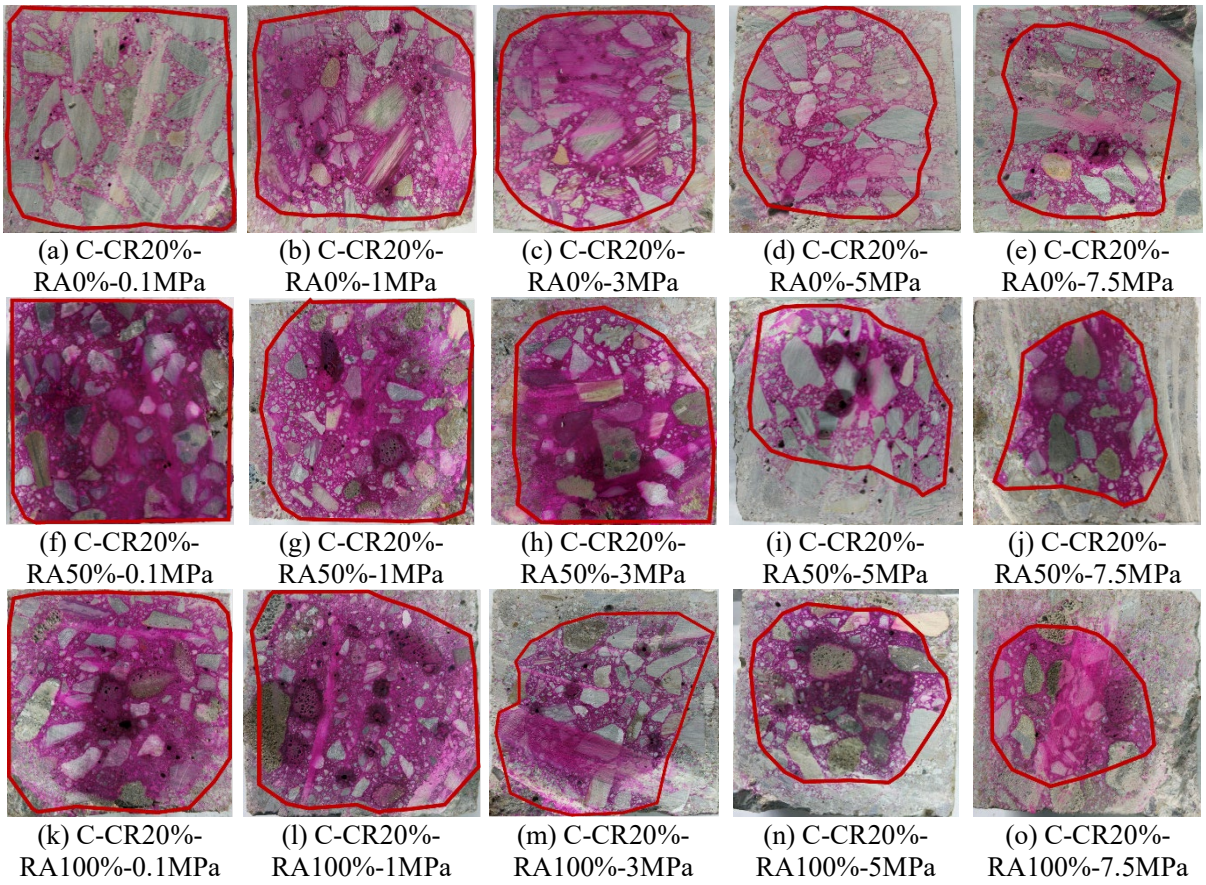

Fig. 10. Carbonation morphology of LCRC under different external CO_2 pressures.

As the external CO_2 pressure increased from 0.1 MPa to 7.5 MPa, as shown in Figs. 10(k)-(o), the carbonation front of LCRC rapidly migrated from the surface toward the internal zone, with a corresponding significant expansion of the colorless carbonation region. Fig. 11 shows that under identical RA replacement ratios, the carbonation depth of LCRC exhibits nonlinear growth with increasing external CO_2 pressure. At 1.0, 3.0, 5.0, and 7.5 MPa, the average carbonation depth of the LCRC increased by 19%, 50%, 83%, and 164%, respectively, compared with at 0.1 MPa. Within the high-pressure range of 5.0-7.5 MPa, the growth rate of carbonation depth markedly exceeds that observed under lower pressure such as 1.0-3.0 MPa and 3.0-5.0 MPa. For the LCRC with RA replacement ratios of 0% and 50% (Figs. 11a and b), the carbonation depth at 7.5 MPa increased by an average of 144% and 165%, respectively, compared to at 0.1 MPa. When the RA replacement ratio was further increased to 100% (Fig. 11c), the carbonation depth at external CO_2 pressure of 7.5 MPa increased by an average of 181% compared to at 0.1 MPa. This difference primarily stems from the interconnected pore structure introduced by the RA, which provides more efficient diffusion pathways for CO_2 under high pressure, significantly reducing gas transport resistance within the LCRC [66]. Under supercritical CO_2 conditions, pressure gradients become the primary driving force for gas transport. This not only accelerates CO_2 molecule penetration into the LCRC but also substantially enhances its solubility in the pore fluid, thereby accelerating the overall carbonation reaction process [67]. This study quantitatively reveals the enhancement effect of supercritical CO_2 pressure on the carbonation depth of LCRC for the first time, providing a theoretical basis for improving the carbon sequestration efficiency of LCRC by pressurized carbonation technology.

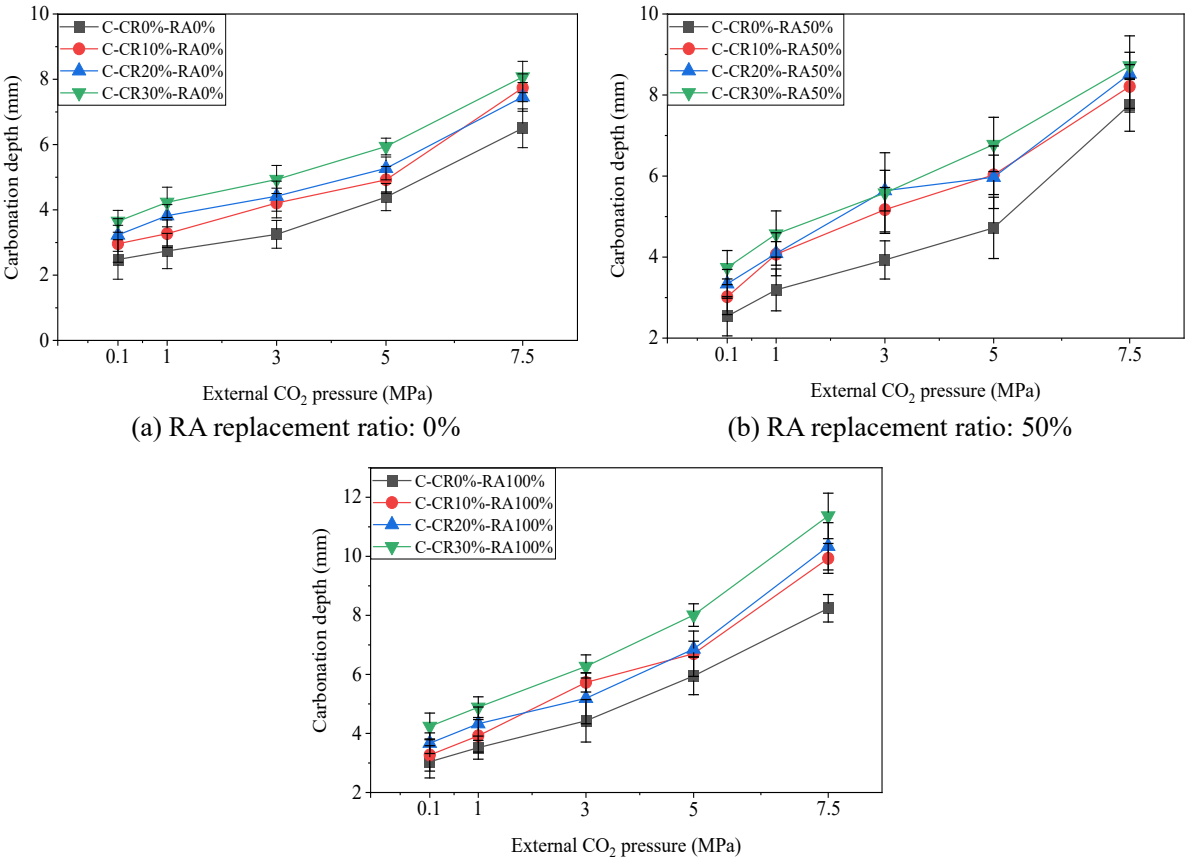

(a) RA replacement ratio: 0%

(b) RA replacement ratio: 50%

(c) RA replacement ratio: 100%

Fig. 11. Carbonation depth of LCRC under different external CO_2 pressure.

3.2. *Pattern of LCRC compressive strength variation*

3.2.1. *Effect of RA replacement ratio*

To investigate the effect of different RA replacement ratios on the compressive strength of LCRC, specimens were selected from both uncarbonated and externally pressurized carbonation conditions. Following the concrete mechanical property testing method outlined in Section 2.6, the average compressive strength and standard deviation of the LCRC were calculated and are presented in Fig. 12. Under the uncarbonated condition and external CO_2 pressures of 0.1 MPa, 1.0 MPa, 3.0 MPa, 5.0 MPa, and 7.5 MPa, the compressive strength of the LCRC exhibited a decreasing trend with increasing RA replacement ratio. As shown in Fig. 12(a), under the uncarbonated condition, the compressive strength of the LCRC decreased significantly with increasing RA replacement ratio. At 100% RA replacement, the compressive strength of the LCRC was 20.3 MPa, representing a 57% decrease compared to the strength of LCRC with 0% RA replacement (47.7 MPa). As shown in Figs. 12(b)-(f), under different CO_2 pressure conditions, the strength reduction was particularly pronounced when the RA replacement ratio increased from 50% to 100%. Compared to the LCRC without RA, the average strength decreases were 12% and 29%, respectively. This phenomenon is primarily attributed to the low density and high porosity of RA. They introduce more initial defects and weak zones into the LCRC matrix, reducing its overall density and adversely affecting its compressive strength [14]. However, this study reveals that the same porous nature of RA that diminishes initial strength simultaneously creates a microstructure that is more responsive to strength enhancement

through carbonation. SEM images (Fig. 15(j)) clearly show that after carbonation (7.5 MPa), dense $CaCO_3$ formed within the pores of the new paste region surrounding the RA, indicating that the porous structure of the aggregate promotes carbonation reactions in the surrounding paste. Consequently, while RA incorporation reduces the compressive strength of LCRC, it also forms a more permeable microstructure that more effectively enhances strength through carbonation.

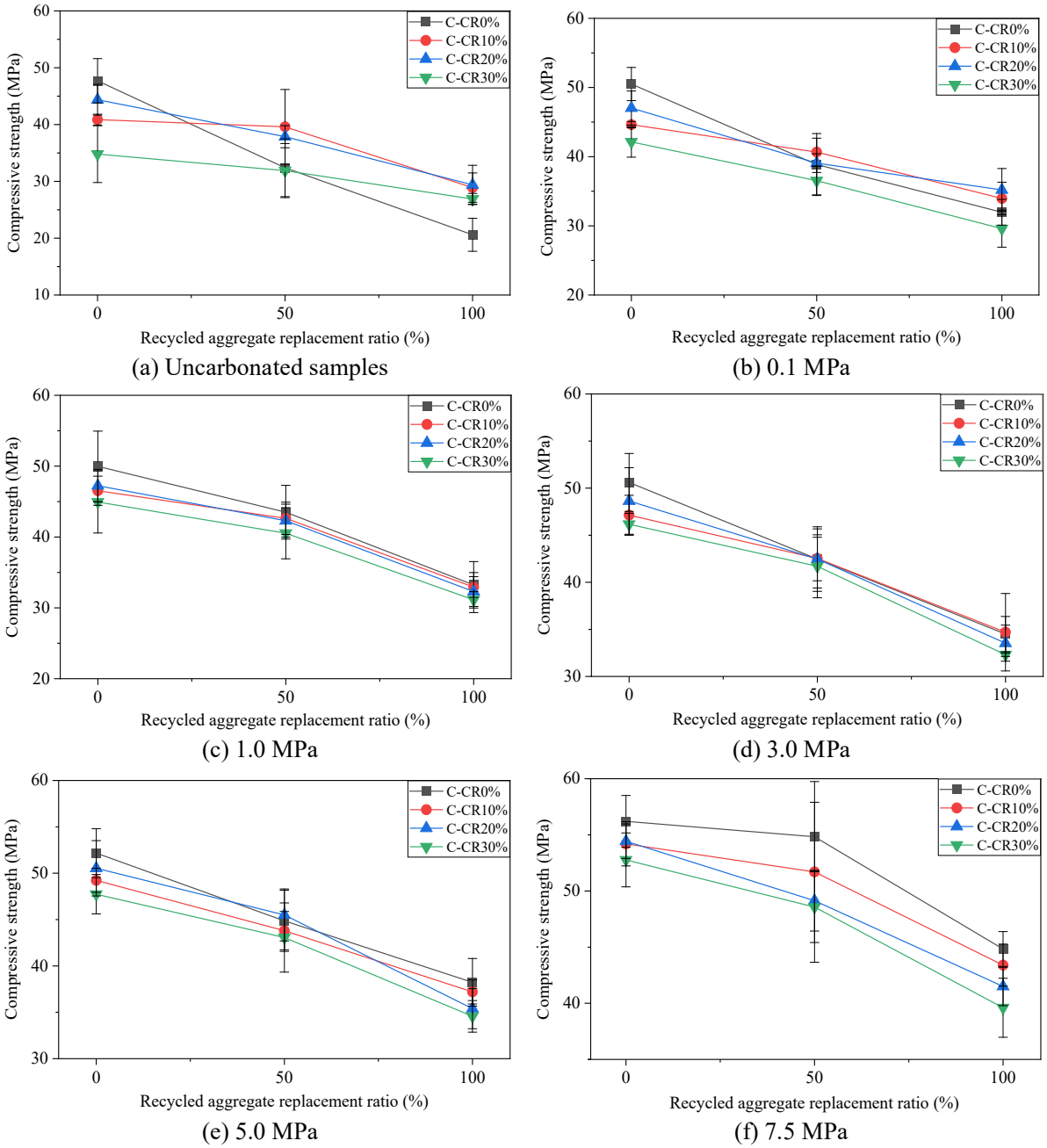

Fig. 12. Compressive strength of LCRC with different RA replacement ratios.

3.2.2. Effect of cement replacement ratio

As shown in Figs. 13(a)-(f), the compressive strength of LCRC exhibits an overall downward trend with increasing cement replacement ratio, though some fluctuations occur locally. Compared to LCRC with 0% cement replacement, specimens with 10%, 20%, and 30% cement replacement exhibited average compressive strength reductions of 3.69%, 3.73%, and 8.34%, respectively. The dilution effect caused by

reduced cement content slowed the hydration reaction rate of LCRC, thereby weakening its matrix strength [68]. Under conditions of 0% RA replacement (Figs. 13a-f), the compressive strength of LCRC fluctuated downward with increasing cement replacement ratio. However, when the RA replacement ratio increased to 50% and 100%, and under non-carbonated conditions with an external CO_2 pressure of 0.1 MPa (Figs. 13a, b), compressive strength improved with increasing cement replacement ratio. This occurred because the physical filling effect of GGBS effectively compensated for the initial defects introduced by RA [69]. As external CO_2 pressure further increased (Figs. 13c-f), the compressive strength of LCRC with RA replacement ratios of 50% and 100% still exhibited an overall decreasing trend with increasing cement replacement ratio. TGA-DSC results (Fig. 18) indicate that the absolute content of $CaCO_3$ formed by carbonation in LCRC decreases with increasing cement replacement ratio. This is because the increased cement replacement ratio depleted the alkaline reserve within the LCRC, thereby reducing the strength-enhancing effect of the carbonation reaction on the LCRC [70]. Notably, the C/Ca atomic ratio significantly increased in post-carbonation specimens. This indicates that, alongside $Ca(OH)_2$, C-S-H gel actively participates in the carbonation reaction and undergoes decalcification, forming amorphous SiO_2 gel. This phenomenon suggests that in LCRC with higher cement replacement ratio, the degree of carbonation reaction is greater but the strength is lower.

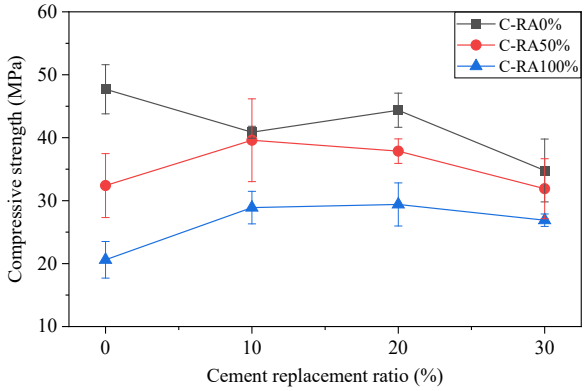

(a) Uncarbonated samples

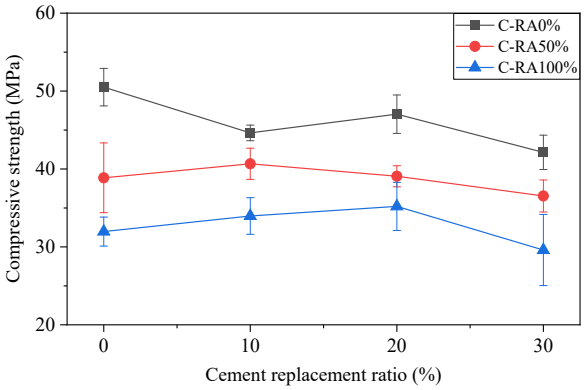

(b) 0.1 MPa

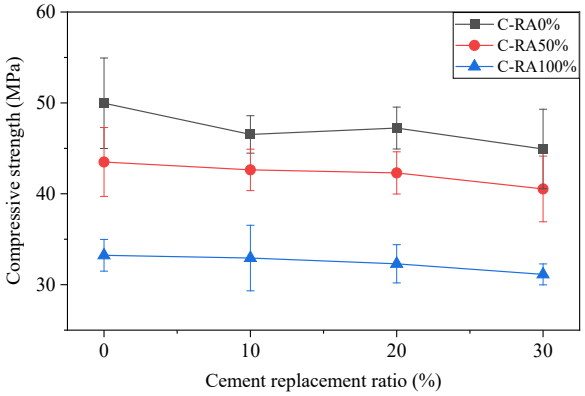

(c) 1.0 MPa

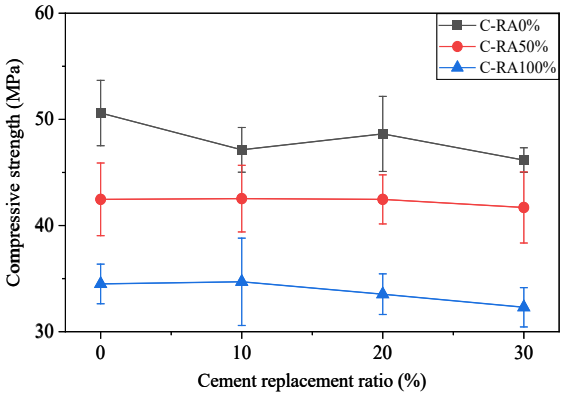

(d) 3.0 MPa

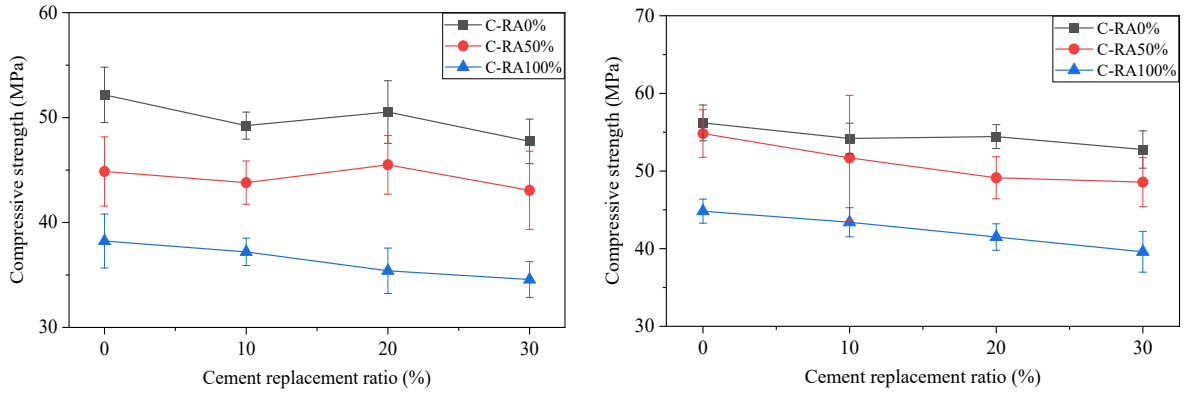

(e) 5.0 MPa (f) 7.5 MPa

Fig. 13. Compressive strength of LCRC under different cement replacement ratios.

3.2.3. Effect of external CO_2 pressure

As illustrated in Figs. 14(a)-(c), when the replacement ratios of RA and cement are the same, the compressive strength of the LCRC is greater if it was carbonated under a higher external CO_2 pressure and reaches its maximum value at 7.5 MPa. Compared with the uncarbonated specimens, the average compressive strength of the LCRC increased by 15%, 19%, 22%, 29%, and 47% after being carbonated under external CO_2 pressures of 0.1, 1.0, 3.0, 5.0, and 7.5 MPa, respectively. When the external CO_2 pressure ranged from 0.1 to 5.0 MPa, the increase in the LCRC compressive strength was relatively gradual. However, the increase in compressive strength significantly accelerated when pressure rose from 5.0 MPa to 7.5 MPa. This is because under the supercritical conditions (7.5 MPa), CO_2 exhibits a density close to that of a liquid and a viscosity close to that of a gas. Consequently, it possesses extremely high diffusion capability and reaction rate within the LCRC, significantly enhancing the carbonation effect and boosting its compressive strength [71]. At a 100% RA replacement ratio, the LCRC specimen had a compressive strength of 44.8 MPa after carbonation at 7.5 MPa, approximately 118% higher than that of its uncarbonated counterpart, which is close to the compressive strength of the uncarbonated NAC with the same mix proportion. This significant enhancement can be explained by the evolution mechanisms of specimen porosity and carbonation products. MIP test results show that the carbonation under external CO_2 pressure of 7.5 MPa reduces the total porosity by 28.49%-33.83% (Fig. 17). The pore size distribution shifted markedly toward smaller pores, resulting in a refined pore structure. In contrast to conventional atmospheric carbonation, which typically forms a dense zone only at the surface and the core performance is relatively weak, supercritical carbonation can promote the thorough carbonization of $Ca(OH)_2$ and C-S-H gel deeper inside the specimen and convert it into $CaCO_3$, thereby reducing the difference in carbonation degree between the surface and the core of the specimen.

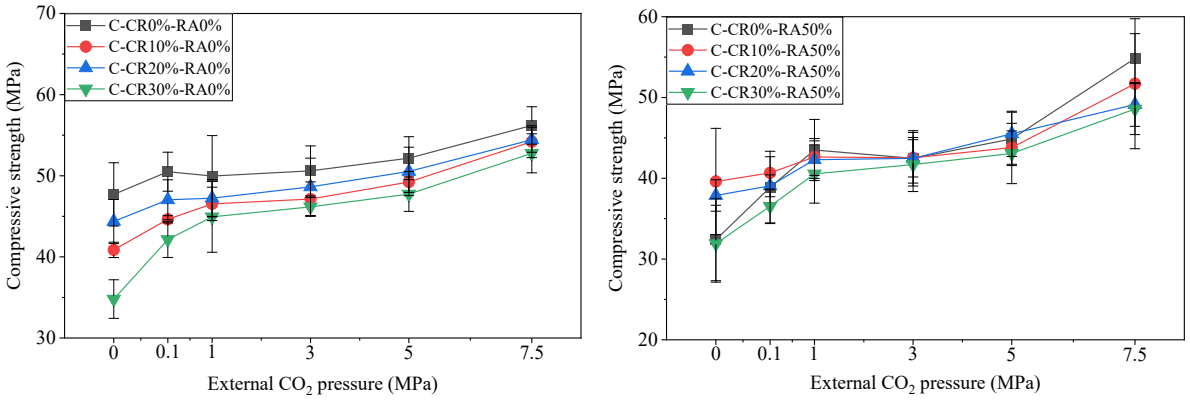

(a) RA replacement ratio: 0%

(b) RA replacement ratio: 50%

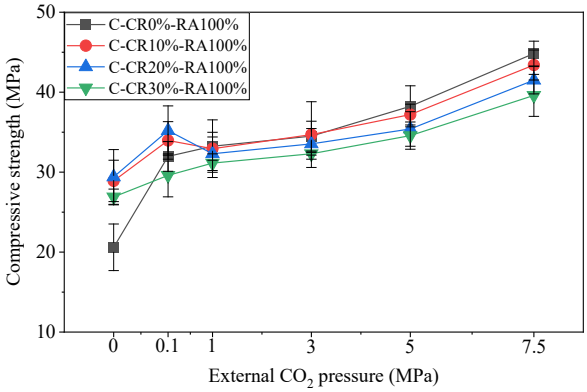

(c) RA replacement ratio: 100%

Fig. 14. Compressive strength of LCRC under different external CO_2 pressures.

3.3. Microstructural and compositional evolution of LCRC under varying CO_2 pressures

3.3.1. Microstructure evolution

To investigate the effects of cement and RA replacement ratios on the pore structure and crystal morphology of LCRC, representative specimens were selected, including those with a RA replacement ratio of 0% and cement replacement ratios of 0%, 10%, 20%, and 30%, as well as a specimen with a RA replacement ratio of 100% and a cement replacement ratio of 10%. The SEM images of the above groups of samples under the uncarbonated condition and external CO_2 pressures of 7.5 MPa are shown in Figs. 15(a)-(j).

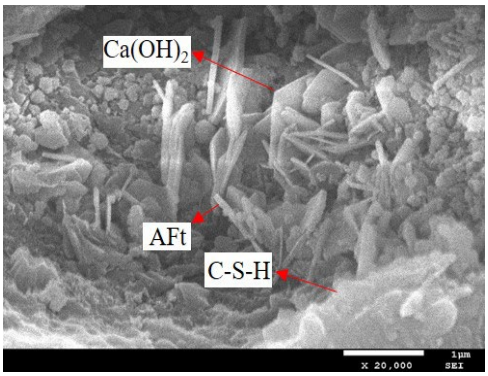

(a) C-CR0%-RA0%-Uncarbonated

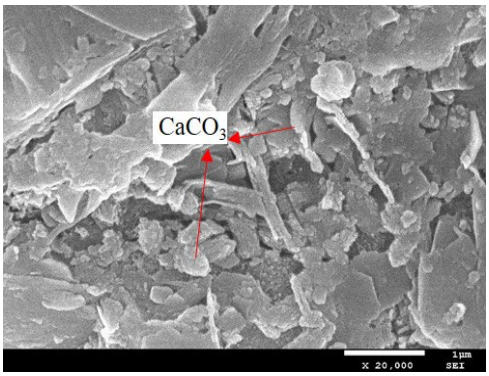

(b) C-CR0%-RA0%-7.5MPa

(c) C-CR10%-RA0%-Uncarbonated

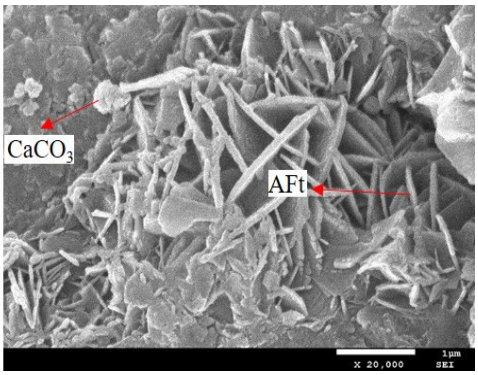

(d) C-CR10%-RA0%-7.5MPa

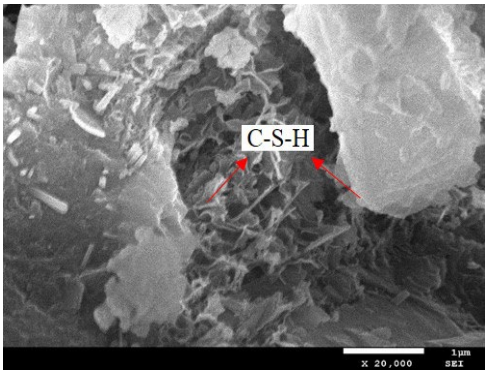

(e) C-CR20%-RA0%-Uncarbonated

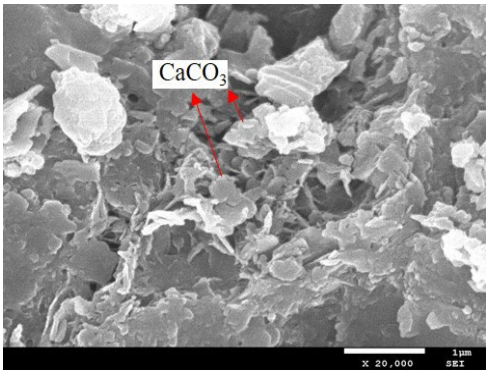

(f) C-CR20%-RA0%-7.5MPa

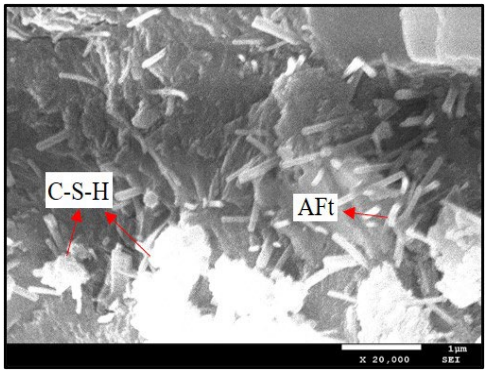

(g) C-CR30%-RA0%-Uncarbonated

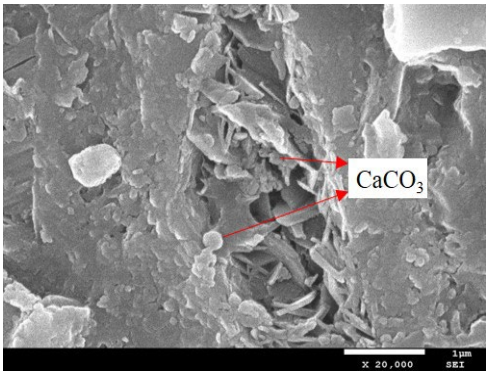

(h) C-CR30%-RA0%-7.5MPa

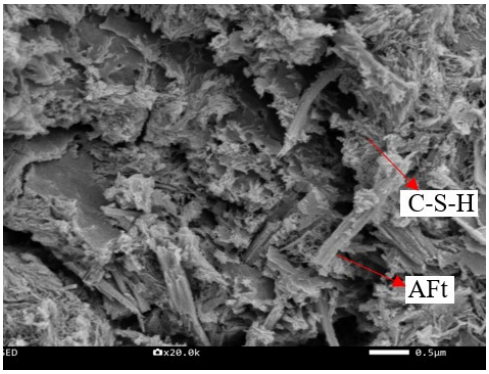

(i) C-CR10%-RA100%-Uncarbonated

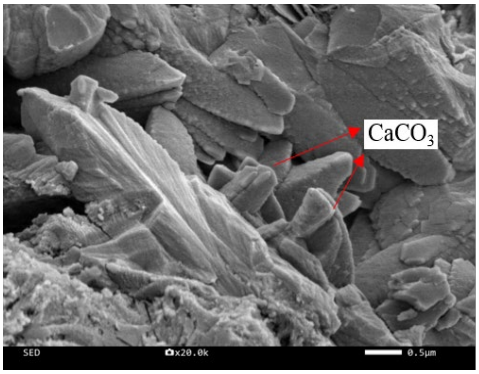

(j) C-CR10%-RA100%-7.5MPa

Fig. 15. SEM images of LCRC specimens.

In the uncarbonated state, the hydration products of the LCRC specimens with cement replacement ratios of 0% and 10% mainly comprise lamellar $Ca(OH)_2$ crystals, flocculent C-S-H gel, and acicular AFt crystals (Fig. 15(a), (c)). As the cement replacement ratio increased to 20% and 30% (Fig. 15(e), (g)), the

amount of $Ca(OH)_2$ generated in the matrix decreased significantly. Only a small amount of needle-like AFt crystals was visible, and the main hydration products shifted to flocculent and reticular C-S-H gel structures. This occurs because the reduced cement content diminishes the system's alkaline reserve, limiting $Ca(OH)_2$ formation. When the RA replacement ratio reaches 100%, the overall morphological characteristics of the hydration products remain largely unchanged. However, the matrix surrounding the RA exhibits a more porous microstructure, as shown in Fig. 15(i). After the 7.5 MPa carbonation treatment (Fig. 15(b), (d), (f), (h)), $Ca(OH)_2$ and C-S-H hydration products were transformed into lamellar and granular $CaCO_3$ crystals, effectively filling pores and significantly enhancing the micro-compactness of the LCRC [72]. In specimens with a 100% RA replacement ratio, post-carbonation microstructural observations reveal a dense accumulation of calcium carbonate crystals in the regions surrounding the RA (Fig. 15(j)). This suggests that the porous structure associated with RA promotes CO_2 transport and reaction, thereby leading to more pronounced deposition of carbonation products at the aggregate-cement paste interface.

To further investigate the degree of carbonation in LCRC under different cement and RA replacement ratios, this study conducted EDX elemental analysis on samples from both carbonated and uncarbonated zones. Figs. 16(a)-(e) present the EDX analysis of the LCRC under the uncarbonated condition and external CO_2 pressures of 7.5 MPa.

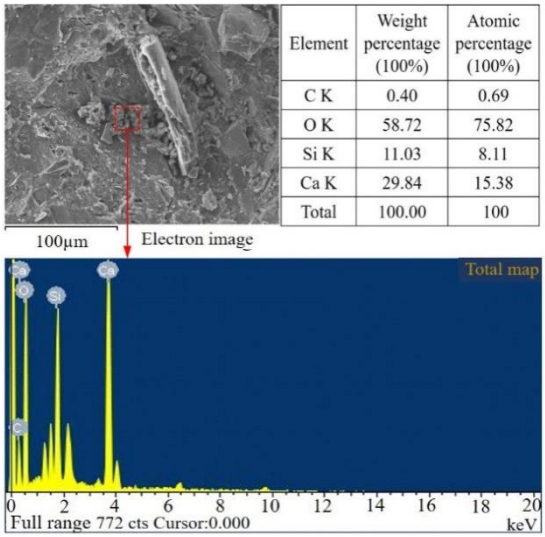

Element	Weight percentage (100%)	Atomic percentage (100%)
C K	0.40	0.69
O K	58.72	75.82
Si K	11.03	8.11
Ca K	29.84	15.38
Total	100.00	100

(a) C-CR0%-RA0%-Uncarbonated

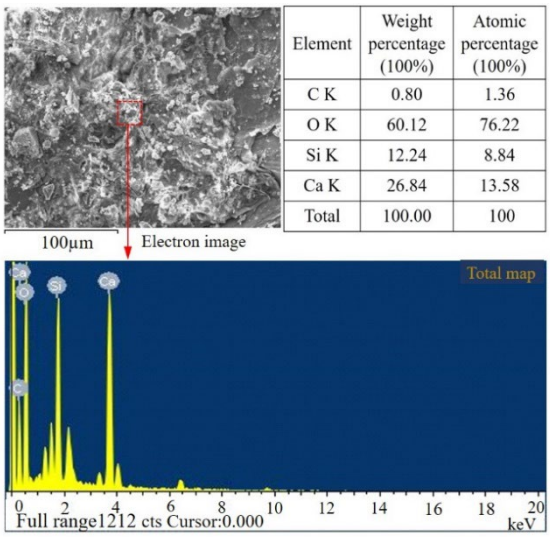

Element	Weight percentage (100%)	Atomic percentage (100%)
C K	0.80	1.36
O K	60.12	76.22
Si K	12.24	8.84
Ca K	26.84	13.58
Total	100.00	100

(b) C-CR0%-RA0%-7.5MPa

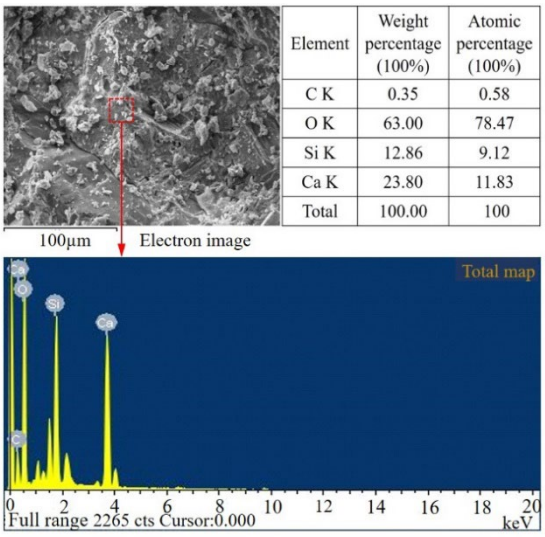

Element	Weight percentage (100%)	Atomic percentage (100%)
C K	0.35	0.58
O K	63.00	78.47
Si K	12.86	9.12
Ca K	23.80	11.83
Total	100.00	100

(c) C-CR30%-RA0%-Uncarbonated

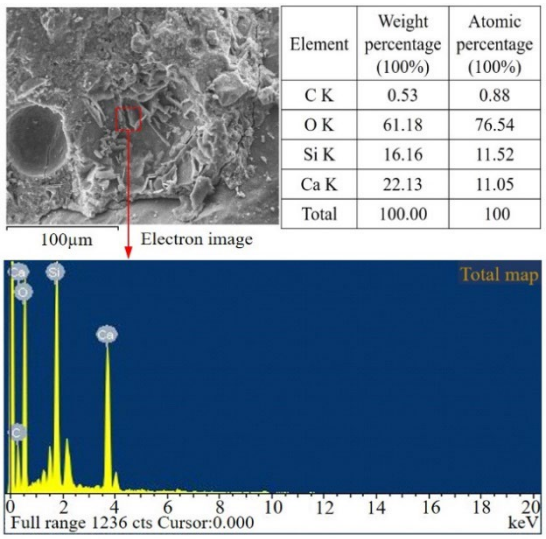

Element	Weight percentage (100%)	Atomic percentage (100%)
C K	0.53	0.88
O K	61.18	76.54
Si K	16.16	11.52
Ca K	22.13	11.05
Total	100.00	100

(d) C-CR30%-RA0%-7.5MPa

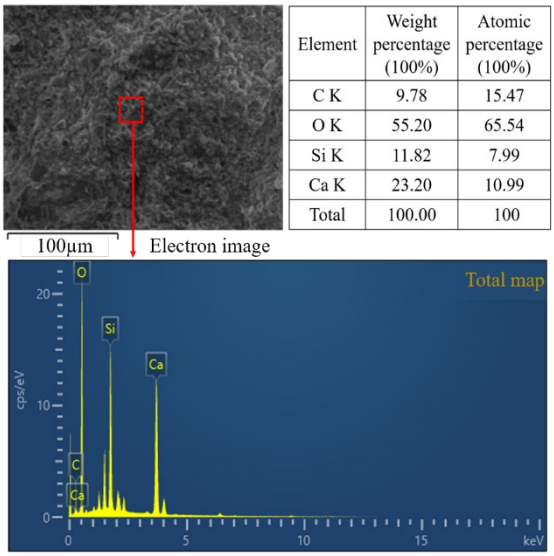

Element	Weight percentage (100%)	Atomic percentage (100%)
C K	9.78	15.47
O K	55.20	65.54
Si K	11.82	7.99
Ca K	23.20	10.99
Total	100.00	100

(e) C-CR10%-RA100%-Uncarbonated

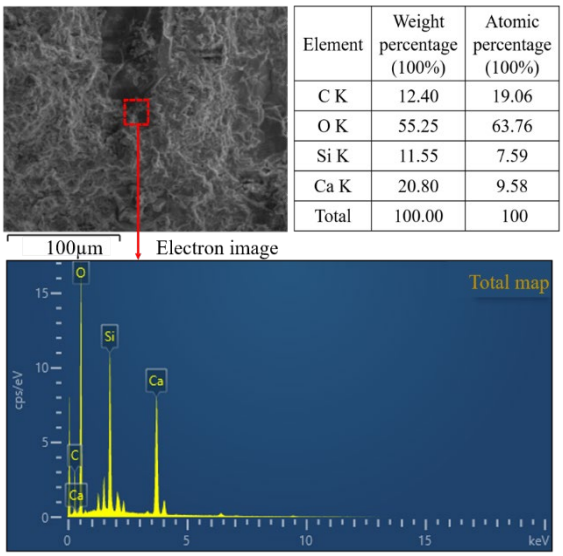

Element	Weight percentage (100%)	Atomic percentage (100%)
C K	12.40	19.06
O K	55.25	63.76
Si K	11.55	7.59
Ca K	20.80	9.58
Total	100.00	100

(f) C-CR10%-RA100%-7.5MPa

Fig. 16. EDX element analysis of LCRC specimens.

Under the uncarbonated condition, the Si/Ca atomic ratio in the 30% cement replacement sample increased by 46% compared to the 0% cement replacement LCRC sample. This primarily resulted from the reduced cement content that decreased $Ca(OH)_2$ content in the system, while the pozzolanic reaction of the GGBS generated more C-S-H gel, further consuming free Ca elements. After carbonation at 7.5 MPa, the C atom ratio in the 0% cement replacement sample increased significantly by 97% compared to at the uncarbonated condition, while the 30% cement replacement sample only increased by 52%. This indicates that a higher cement replacement ratio limits the total amount of $Ca(OH)_2$ available for carbonation reactions, thereby inhibiting $CaCO_3$ formation [73]. Furthermore, the C/Ca atom ratio in both the 0% and 30% cement replacement samples was higher than that in the uncarbonated samples after carbonation, indicating that C-S-H gel also participated in the carbonation reaction process alongside $Ca(OH)_2$. EDX analysis of LCRC specimens with 100% RA replacement ratio and a 10% cement replacement ratio before and after carbonation shows that carbonation at 7.5 MPa increases the atomic percentage of C by up to 23.2%, confirming a

synergistic effect between the highly porous RA and elevated CO_2 pressure. Meanwhile, the Si/Ca atomic ratio remains relatively stable after carbonation, indicating that a low cement replacement ratio plays a regulatory role in maintaining alkali reserves and preventing structural imbalance caused by excessive consumption of Ca-bearing phases.

3.3.2. Porosity variation

To investigate the effects of cement and RA replacement ratios on the porosity of LCRC, representative specimens were selected, including those with a RA replacement ratio of 0% and cement replacement ratios of 0%, 10%, 20%, and 30%, as well as a specimen with a RA replacement ratio of 100% and a cement replacement ratio of 10%. The cumulative mercury intrusion curves of the LCRC specimens under the uncarbonated condition and external CO_2 pressures of 7.5 MPa are shown in Fig. 17, respectively, and the porosity test data for the LCRC before and after carbonation are summarized in Table 7.

Under the uncarbonated condition, the total porosity of the LCRC specimens containing 0% RA exhibits an increasing trend with higher cement replacement ratios. This is primarily attributed to the slower early-stage hydration rate of GGBS, which facilitates the formation of interconnected pores ranging from 1 to 5 μm in size between unreacted particles, thereby enhancing the overall porosity. Analyzing different pore size distributions reveals that at 0% cement replacement, macropores (>1000 nm) accounted for 35% of the totals. When cement replacement reached 10%, 20%, and 30%, macropores percentage are 49%, 19%, and 26%, respectively. This is due to the physical filling effect of the GGBS, which refines the pore structure within the LCRC [69]. When the RA replacement ratio reaches 100%, the high porosity and water absorption characteristics of RA result in an initial porosity of the LCRC specimens that is 12.2% higher compared to specimens with a 0% RA replacement ratio. Under external CO_2 pressure of 7.5 MPa, the total porosity of the LCRC specimens with 0% RA replacement decreased by 28.94%-33.83% compared to at the uncarbonated state, with the most significant reduction observed in specimens with 30% cement replacement. For LCRC specimens with 100% RA replacement, the porosity decreased by 29.59% after carbonation, exceeding the reduction observed in specimens with 0% RA replacement. This is closely related to its highest initial porosity: more initial voids provided ample space for the precipitation and filling of the carbonation product $CaCO_3$, thereby amplifying the pore optimization effect of the carbonation reaction [42].

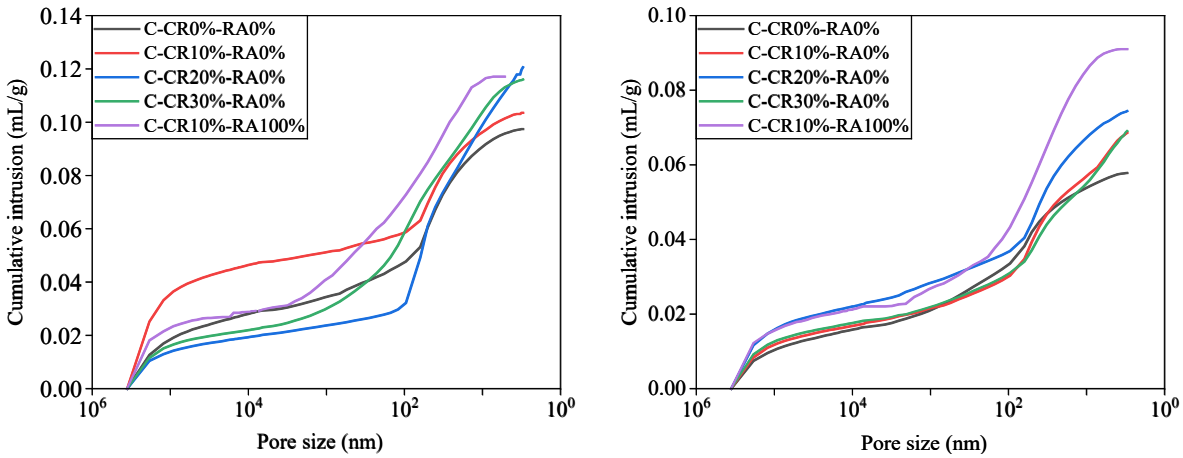

(a) Uncarbonated samples (b) 7.5 MPa

Fig. 17. MIP test results of LCRC before and after carbonation.

Table 7 Porosity of LCRC specimens before and after carbonation.

Groups	Porosity before carbonation	Porosity after carbonation	Ratio of decrement
C-CR0%-RA0%	18.41%	12.52%	32%
C-CR10%-RA0%	19.24%	13.66%	29%
C-CR20%-RA0%	20.08%	14.36%	28.49%
C-CR30%-RA0%	21.58%	14.28%	33.83%
C-CR10%-RA100%	23.89%	16.82%	29.59%

Remarks: Porosity values are the total intrusion porosity obtained from MIP measurements.

3.3.3. Contents of $Ca(OH)_2$ and C-S-H

To investigate changes in $CaCO_3$ and $Ca(OH)_2$ content in the carbonate and uncarbonated zones of LCRC under varying CO_2 pressures, representative LCRC specimens were selected for testing: specimens with 0% RA replacement ratio and 0% or 30% cement replacement ratio, as well as specimens with 100% RA replacement ratio and 10% cement replacement ratio. Fig. 18 displays the TGA-DSC curves of these specimens after carbonation under external CO_2 pressures of 0.1 MPa and 7.5 MPa, as well as under the uncarbonated condition. The figure reveals that for all the carbonated specimens, the DSC curves exhibit significantly weakened peaks characterizing $Ca(OH)_2$ decomposition within the 400-500°C range, while the peaks indicating $CaCO_3$ decomposition within the 600-800°C range are markedly enhanced. This indicates that the carbonation reaction converts hydration products such as $Ca(OH)_2$ into $CaCO_3$ [74].

When the RA and cement replacement ratio were both 0% (Fig. 18a), the $CaCO_3$ mass fraction after 7.5 MPa carbonation reached 8.26%, an increase of 18.3% compared to the 0.1 MPa condition, indicating that high pressure significantly promoted the formation of carbonation products. However, when the cement replacement ratio increased to 30% (Fig. 18b), the $Ca(OH)_2$ content in the uncarbonated sample was 1.03%, lower than the 1.28% observed in the sample with 0% cement replacement. This is primarily due to the reduced cement content and its slowed hydration rate, leading to decreased $Ca(OH)_2$ formation [75]. After carbonation at 7.5 MPa, the $CaCO_3$ content in this group of samples was 5.91%, representing a 28.5% decrease compared to samples with 0% cement replacement. This reduction is attributed to insufficient initial $Ca(OH)_2$ and the further consumption of Ca^{2+} by the GGBS pozzolanic reaction. At 100% RA replacement, the $CaCO_3$ mass fraction after 7.5 MPa carbonation reached 10.59%, a 28.2% increase compared to the 0% RA and cement replacement samples. This directly demonstrates that RA's high porosity provides efficient transport pathways for supercritical CO_2, whose synergistic interaction with the high-pressure environment significantly accelerates the deposition of carbonation products and pore filling, thereby establishing a microscopic foundation for enhancing macroscopic compressive strength.

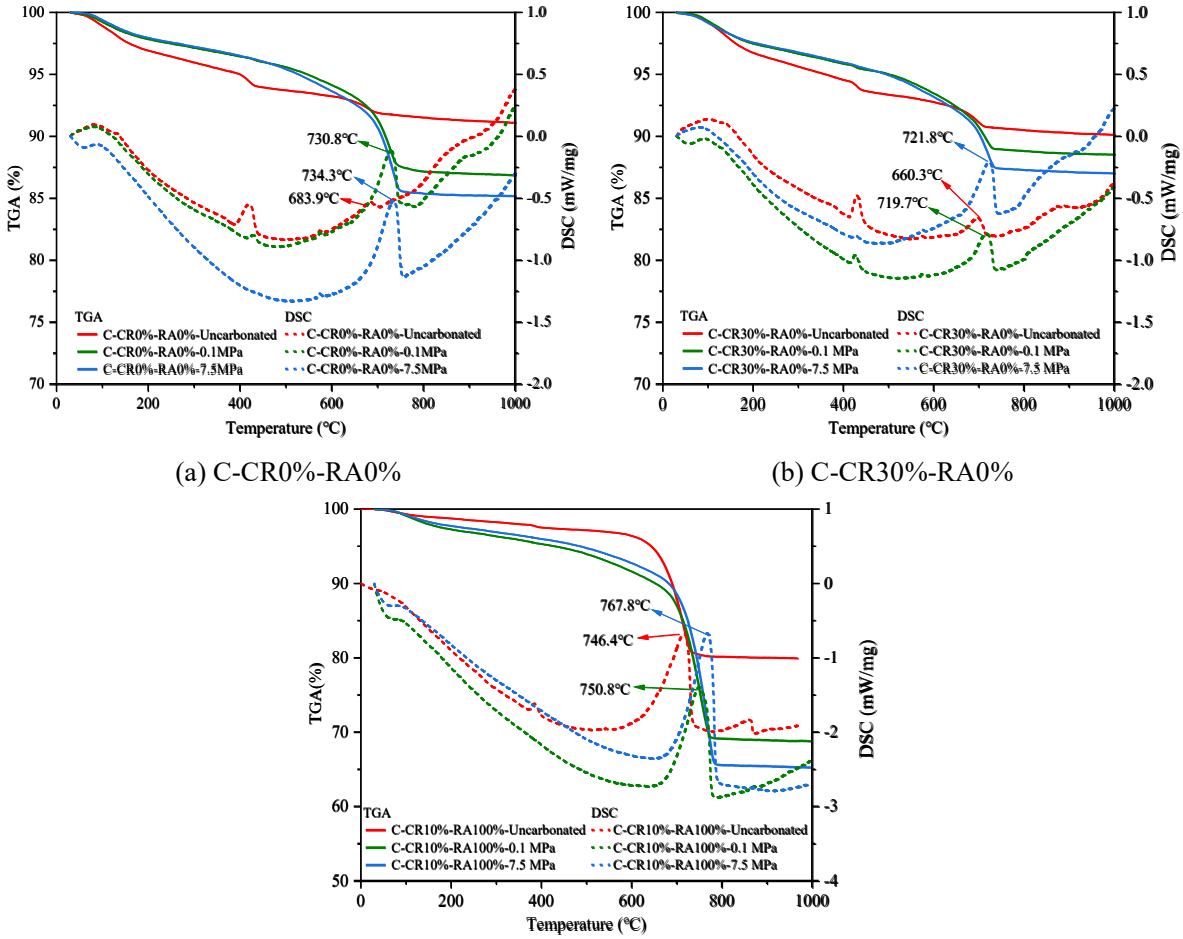

(a) C-CR0%-RA0%

(b) C-CR30%-RA0%

(c) C-CR10%-RA100%

Fig. 18. TGA-DSC results of LCRC before and after carbonation.

The $Ca(OH)_2$ and C-S-H contents in the cementitious material prior to carbonation were determined using the method. These values were compared with the C-S-H and $Ca(OH)_2$ contents calculated from other literature sources [76-81], as shown in Fig. 19. The results indicate that in most studies, the C-S-H content ranged from 60% to 83%, while $Ca(OH)_2$ content was found to be in the range of 17% to 40%.

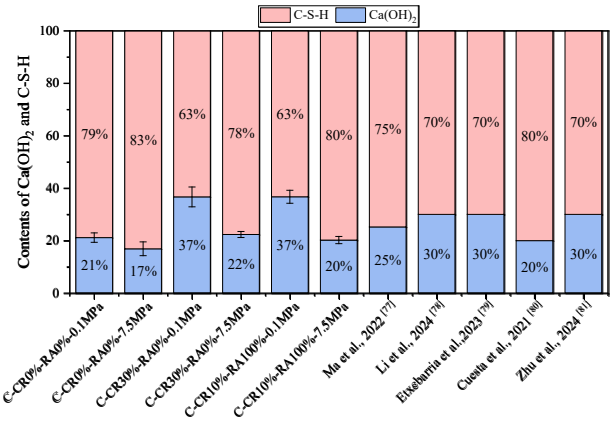

Fig. 19. C-S-H and $Ca(OH)_2$ content in cementitious materials before carbonation.

3.3.4. CO_2 uptake capacity

To evaluate the CO_2 uptake capacity of fully carbonated cementitious materials, this study calculated the CO_2 uptake capacity of LCRC using Eq. (10) based on the TGA mass loss in the temperature range of 600-800°C shown in Fig. 18. The results indicate that under external CO_2 pressures of 0.1 MPa and 7.5 MPa, the average CO_2 uptake capacity of the LCRC specimens with cement replacement ratios of 0% and 30% was 42.23 kg/m^3. Notably, when the RA replacement ratio reached 100% and the cement replacement ratio was 10%, the LCRC achieved its peak CO_2 uptake capacity of 96.09 kg/m^3 under external CO_2 pressure of 7.5 MPa. This represents a significant increase of approximately 49.6% compared to specimens with 0% RA and 0% cement replacement ratios. This indicates that the porous structure of RA provides an efficient transport pathway for supercritical CO_2, enabling its rapid penetration into the material interior. This simultaneously maximizes both CO_2 sequestration efficiency and microstructural reinforcement. At the same time, the material composition also plays a crucial regulatory role. Although increasing cement replacement ratios reduces carbon emissions during concrete production, it also diminishes its CO_2 uptake capacity. The CO_2 uptake capacity of LCRC with a 30% cement replacement ratio decreased by 22.8% after carbonation at 7.5 MPa compared to that of cement with a 0% replacement ratio. This indicates that a balance must be struck between maximizing carbon sequestration and reducing cement usage. Finally, the calculated results are compared in Fig. 20 with data from other studies [82-87].

$$m_{CO_2} = \frac{(D_{800} - D_{600}) \times m_C}{M_{CC}} \times M_{CO_2} \tag{10}$$

where m_{CO2} is the mass of carbon dioxide absorbed per cubic meter of concrete, m_c is the mass per unit volume of LCRC, which is calculated as the bulk density (2100-2400 kg/m^3) of the specific mix design, and M_{CO2} is the molar mass of CO_2 (44 g/mol).

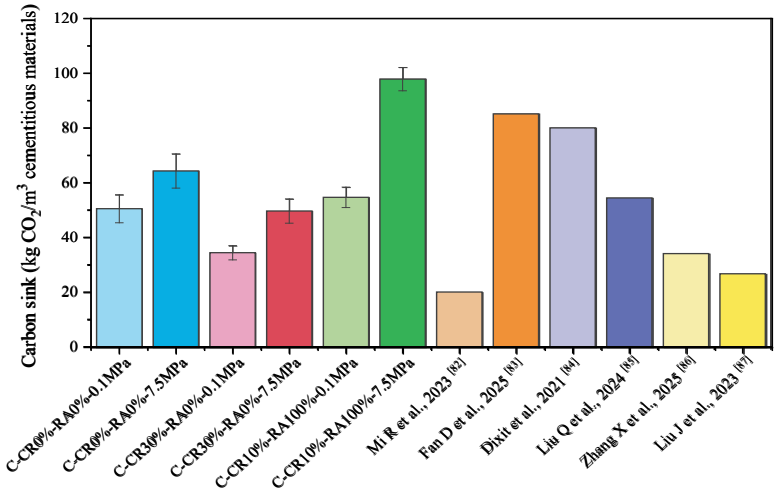

Fig. 20. CO_2 uptake of cementitious materials after completely carbonation.

3.4. Accelerated carbonation mechanism of LCRC

In this study, the accelerated carbonation mechanism of LCRC under different CO_2 pressures was studied by means of SEM, MIP, and TGA-DSC, the essence of which is a pressure-driven physical and chemical coupling process [72] as shown in Fig. 21.

Increased external CO_2 pressure first creates a pressure gradient within the concrete, accelerating CO_2 transport and elevating its concentration within pores. Simultaneously, this process promotes the migration of water within the concrete toward micro-pores, thereby exposing a larger gas-liquid reaction interface. At this expanded interface, the dissolution reaction rate of CO_2 significantly increases; where it dissolves to forms H_2CO_3, which then decompose into HCO_3^- and CO_3^{2-}. The increase of CO_3^{2-} concentration not only accelerates the reaction with Ca^{2+} dissolved from $Ca(OH)_2$ in the pore solution but also promotes the decalcification and decomposition of C-S-H gel to produce more $CaCO_3$ and amorphous SiO_2. This was confirmed by the consumption of $Ca(OH)_2$, the formation of $CaCO_3$ and the increase of C/Ca atomic ratio in TGA-DSC and EDX analysis. The $CaCO_3$ crystals generated by the reaction effectively filled the pores and ITZ of the concrete. The MIP test showed that the total porosity could be reduced by about 30% after carbonation. The densification of this microstructure is the fundamental reason for the improvement of macroscopic compressive strength. However, high pressure and high carbonation may also lead to partial deconstruction of the C-S-H gel structure, and their effect on long-term durability needs further study.

Under atmospheric pressure conditions, concrete carbonation is primarily governed by CO_2 diffusion driven by concentration gradients, resulting in a relatively slow process dominated by surface reactions [24, 88, 89]. In contrast, increasing external CO_2 pressure fundamentally alters the carbonation mechanism. Elevated CO_2 pressure significantly accelerates carbonation and increases its depth by enhancing the coupled processes of CO_2 transport, dissolution, and reaction. In this case, the pressure gradient, rather than the concentration gradient, becomes the dominant driving force, promoting CO_2 penetration and dissolution within the concrete matrix. This process facilitates the formation of $CaCO_3$ and pore-filling effects, thereby optimizing the microstructure and ultimately enhancing the mechanical properties of LCRC while enabling effective CO_2 sequestration.

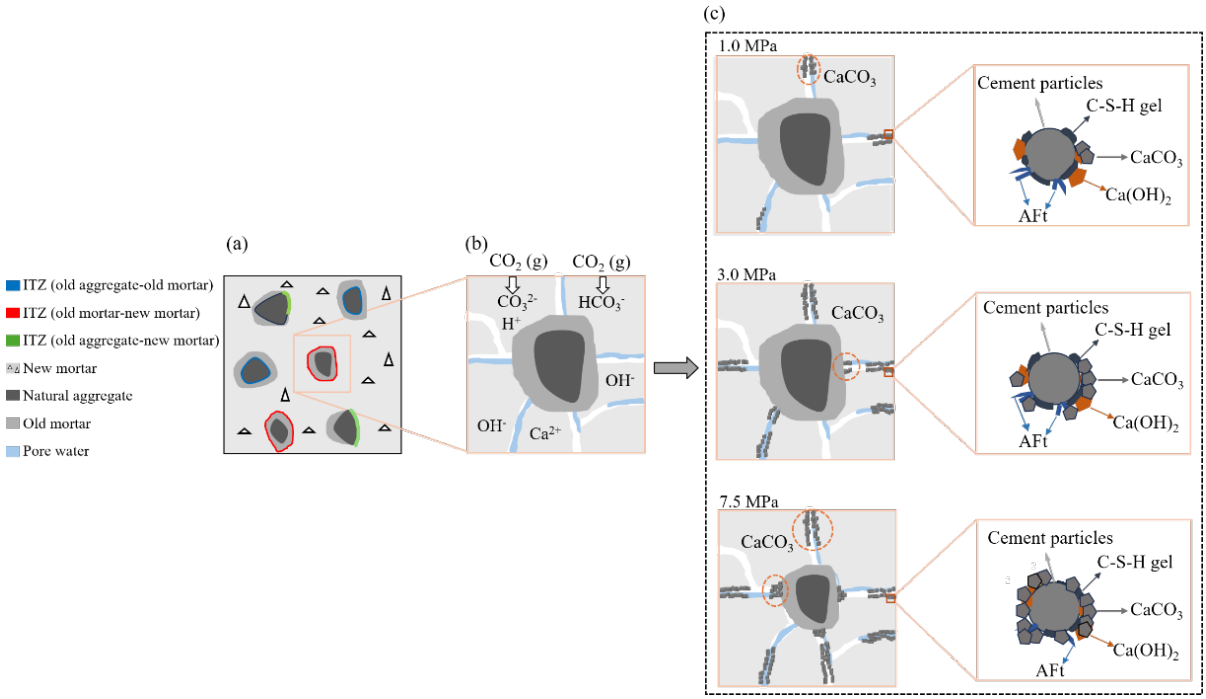

Fig. 21. The carbonation reaction mechanism of LCRC under different external CO_2 pressure. (a) The phase composition of cementitious materials; (b) CO_2 transport and reactions in pore fluids; (c) The conversion

process of hydration products to $CaCO_3$.

4. Conclusions

This study investigated the effects of RA replacement ratio, cement replacement ratio, and external CO_2 pressure on the carbonation depth and compressive strength of LCRC. SEM, MIP, and TGA-DSC analyses were conducted to characterize its microstructural evolution and reveal the accelerated carbonation mechanism.

(1) Increasing RA replacement, cement replacement, and CO_2 pressure all deepen the carbonation depth, of with CO_2 pressure was the dominant factor. At 1.0, 3.0, 5.0, and 7.5 MPa, the carbonation depth of the LCRC increased by 19%, 50%, 83%, and 164%, respectively, compared with at 0.1 MPa.

(2) Increasing RA and cement replacement reduced compressive strength, while elevated CO_2 pressure significantly enhanced the strength. Under the same pressure condition, the compressive strength increased by 15%, 19%, 22%, 29%, and 47% respectively compared with the uncarbonated specimen.

(3) During carbonation, flocculent C-S-H gels in the matrix and interfacial zones was transformed into $CaCO_3$, refining the pore structure and reducing total porosity by 28%-34%.

(4) TGA-DSC results indicated that pre-carbonation C-S-H and $Ca(OH)_2$ contents were 63%-83% and 17%-37%, respectively. The maximum CO_2 uptake capacity was about 96.09 kg CO_2/m^3.

(5) Increasing CO_2 pressure accelerated gas transport and dissolution, promoted C-S-H decalcification and $CaCO_3$ formation, and enhanced both pore densification and CO_2 uptake efficiency.

CRediT authorship contribution statement

Hao Bao: Conceptualization, Methodology, Supervision, Validation, Visualization, Writing-review & editing. **Jie Wang:** Data curation, Investigation, Validation, Writing-original draft. **Gang Xu:** Supervision. **Ruyu Wang:** Data curation, Investigation. **Mohamed Saafi:** Supervision. **Jianqiao Ye:** Supervision, Visualization, Writing-review & editing.

Declaration of Interest Statement

The authors declare that they have no known competing financial interests or personal relationships that could have appeared to influence the work reported in this article.

Acknowledgements

The authors are grateful for the financial support from the National Natural Science Foundation of China (Grant No. 52308266), as well as the Future City Research Institute (FCRI) Flagship Program and the Royal Society (Grant: IEC\NSFC\191350).

Data availability statement

Data can be available upon reasonable request to the corresponding author.

References

[1] R. Warburton, Global warming has concrete problem when it comes to CO_2, EcoRi News 25 (2019).
[2] N. Deutscher, Global cement production from 1990 to 2030 (in million metric tons), Statista GmbH (Hamburg) (2019).
[3] Y. Ju, H. Zhang, D. Wang, et al., Effect of mineral admixtures on the resistance to sulfate attack of reactive

656 powder concrete, Journal of Cleaner Production 440 (2024) 140769.
657 http://10.1016/j.jclepro.2024.140769
658 [4] P.O. Awoyera, B.F. Britto, Foamed concrete incorporating mineral admixtures and pulverized ceramics:
659 Effect of phase change and mineralogy on strength characteristics, Construction and Building Materials
660 234 (2020) 117434. http://10.1016/j.conbuildmat.2019.117434
661 [5] L. Wu, Z. Sun, Y. Cao, Modification of recycled aggregate and conservation and application of recycled
662 aggregate concrete: A review, Construction and Building Materials 431 (2024).
663 http://10.1016/j.conbuildmat.2024.136567
664 [6] B.I. Oluleye, D.W.M. Chan, T.O. Olawumi, Barriers to circular economy adoption and concomitant
665 implementation strategies in building construction and demolition waste management: A PRISMA and
666 interpretive structural modeling approach, Habitat International 126 (2022).
667 http://10.1016/j.habitatint.2022.102615
668 [7] R.V. Silva, J. de Brito, R.K. Dhir, Use of recycled aggregates arising from construction and demolition
669 waste in new construction applications, Journal of Cleaner Production 236 (2019).
670 http://10.1016/j.jclepro.2019.117629
671 [8] A. Singh, X. Miao, X. Zhou, et al., Use of recycled fine aggregates and recycled powders in sustainable
672 recycled concrete, Journal of Building Engineering 77 (2023). http://10.1016/j.jobe.2023.107370
673 [9] S. Jamil, J. Shi, M. Idrees, Effect of various parameters on carbonation treatment of recycled concrete
674 aggregate using the design of experiment method, Construction and Building Materials 382 (2023)
675 131339. http://10.1016/j.conbuildmat.2023.131339
676 [10] F. Winnefeld, A. Leemann, A. German, et al., CO_2 storage in cement and concrete by mineral carbonation,
677 Current Opinion in Green and Sustainable Chemistry 38 (2022) 100672.
678 http://10.1016/j.cogsc.2022.100672
679 [11] Z. Duan, A. Singh, J. Xiao, et al., Combined use of recycled powder and recycled coarse aggregate
680 derived from construction and demolition waste in self-compacting concrete, Construction and Building
681 Materials 254 (2020) 119323. http://10.1016/j.conbuildmat.2020.119323
682 [12] G. Bai, C. Zhu, C. Liu, et al., An evaluation of the recycled aggregate characteristics and the recycled
683 aggregate concrete mechanical properties, Construction and building materials 240 (2020) 117978.
684 http://10.1016/j.conbuildmat.2019.117978
685 [13] B. Wang, L. Yan, Q. Fu, et al., A Comprehensive Review on Recycled Aggregate and Recycled
686 Aggregate Concrete, Resources, Conservation and Recycling 171 (2021) 105565.
687 http://10.1016/j.resconrec.2021.105565
688 [14] J. Wang, J. Zhang, D. Cao, Pore characteristics of recycled aggregate concrete and its relationship with
689 durability under complex environmental factors, Construction and Building Materials 272 (2021)
690 121642. http://10.1016/j.conbuildmat.2020.121642
691 [15] X. Liu, X. Xie, R. Liu, et al., Research on the durability of nano-SiO_2 and sodium silicate co-modified
692 recycled coarse aggregate (RCA) concrete, Construction and Building Materials 378 (2023) 131185.
693 http://10.1016/j.conbuildmat.2023.131185
694 [16] A.A. Bahraq, J. Jose, M. Shameem, et al., A review on treatment techniques to improve the durability of
695 recycled aggregate concrete: Enhancement mechanisms, performance and cost analysis, Journal of
696 Building Engineering 55 (2022) 104713. http://10.1016/j.jobe.2022.104713
697 [17] J. Xiao, B. Lei, C. Zhang, On carbonation behavior of recycled aggregate concrete, Science China
698 Technological Sciences 55(9) (2012) 2609-2616. http://10.1007/s11431-012-4798-5
699 [18] Y. Li, T. Fu, R. Wang, et al., An assessment of microcracks in the interfacial transition zone of recycled
700 concrete aggregates cured by CO_2, Construction and Building Materials 236 (2020) 117543.
701 http://10.1016/j.conbuildmat.2019.117543
702 [19] B. Lu, C. Shi, Z. Cao, et al., Effect of carbonated coarse recycled concrete aggregate on the properties
703 and microstructure of recycled concrete, Journal of Cleaner Production 233 (2019) 421-428.
704 http://10.1016/j.jclepro.2019.05.350
705 [20] B. Tang, M. Fan, Z. Yang, et al., A comparison study of aggregate carbonation and concrete carbonation
706 for the enhancement of recycled aggregate pervious concrete, Construction and Building Materials 371
707 (2023) 130797. http://10.1016/j.conbuildmat.2023.130797
708 [21] R. Silva, R. Neves, J. De Brito, et al., Carbonation behaviour of recycled aggregate concrete, Cement
709 and Concrete Composites 62 (2015) 22-32. http://doi.org/10.1016/j.cemconcomp.2015.04.017
710 [22] N.K. Bui, T. Satomi, H. Takahashi, Mechanical properties of concrete containing 100% treated coarse
711 recycled concrete aggregate, Construction and Building Materials 163 (2018) 496-507.
712 http://10.1016/j.conbuildmat.2017.12.131

[23] C. Liang, B. Pan, Z. Ma, et al., Utilization of CO_2 curing to enhance the properties of recycled aggregate and prepared concrete: A review, Cement and concrete composites 105 (2020) 103446. http://10.1016/j.cemconcomp.2019.103446
[24] W. Zuo, X. Zhao, J. Luo, et al., Investigating the impact of carbonation curing concentrations on the mechanical properties and microstructure of recycled concrete, Journal of Building Engineering 96 (2024) 110465. http://10.1016/j.jobe.2024.110465
[25] S. Hang, L. Liang, Y. Huang, et al., Experimental evaluation of mechanical properties and microstructure for recycled aggregate concrete collaboratively modified with nano-silica and mixed fibers, Construction and Building Materials 403 (2023) 133125. http://10.1016/j.conbuildmat.2023.133125
[26] J. Yin, A. Kang, P. Xiao, et al., Influences of spraying sodium silicate based solution/slurry on recycled coarse aggregate, Construction and Building Materials 377 (2023) 130924. http://10.1016/j.conbuildmat.2023.130924
[27] S. Gao, Y. Ji, Z. Qin, et al., A comprehensive analysis of pore structures and performances of mineral admixtures modified recycled aggregate concrete based on experiment and theory, Construction and Building Materials 358 (2022) 129451. http://10.1016/j.conbuildmat.2022.129451
[28] R. Kurda, J. de Brito, J.D. Silvestre, Water absorption and electrical resistivity of concrete with recycled concrete aggregates and fly ash, Cement and Concrete Composites 95 (2019) 169-182. http://10.1016/j.cemconcomp.2018.10.004
[29] N. Bahrami, M. Zohrabi, S.A. Mahmoudy, et al., Optimum recycled concrete aggregate and micro-silica content in self-compacting concrete: Rheological, mechanical and microstructural properties, Journal of building Engineering 31 (2020) 101361. http://10.1016/j.jobe.2020.101361
[30] Y. Wu, H. Mehdizadeh, K.H. Mo, et al., High-temperature CO_2 for accelerating the carbonation of recycled concrete fines, Journal of Building Engineering 52 (2022) 104526. http://10.1016/j.jobe.2022.104526
[31] C. Wang, J. Wang, X. Liu, et al., Orthogonal experimental design for compressive strength of recycled coarse aggregate concrete with silica fume-slag-fly ash hybrid micro-powders, Construction and Building Materials 408 (2023) 133669. http://10.1016/j.conbuildmat.2023.133669
[32] M.S. Rais, R.A. Khan, Experimental investigation on the strength and durability properties of bacterial self-healing recycled aggregate concrete with mineral admixtures, Construction and Building Materials 306 (2021) 124901. http://10.1016/j.conbuildmat.2021.124901
[33] J. Sun, P. Zhang, Effects of different composite mineral admixtures on the early hydration and long-term properties of cement-based materials: A comparative study, Construction and Building Materials 294 (2021) 123547. http://10.1016/j.conbuildmat.2021.123547
[34] J. Wang, Z. Che, K. Zhang, et al., Performance of recycled aggregate concrete with supplementary cementitious materials (fly ash, GBFS, silica fume, and metakaolin): Mechanical properties, pore structure, and water absorption, Construction and Building Materials 368 (2023) 130455. http://10.1016/j.conbuildmat.2023.130455
[35] L.A. Qureshi, B. Ali, A. Ali, Combined effects of supplementary cementitious materials (silica fume, GGBS, fly ash and rice husk ash) and steel fiber on the hardened properties of recycled aggregate concrete, Construction and Building Materials 263 (2020) 120636. http://10.1016/j.conbuildmat.2020.120636
[36] L. Qin, X. Gao, T. Chen, Influence of mineral admixtures on carbonation curing of cement paste, Construction and Building Materials 212 (2019) 653-662. http://10.1016/j.conbuildmat.2019.04.033
[37] T. Chen, M. Bai, X. Gao, Carbonation curing of cement mortars incorporating carbonated fly ash for performance improvement and CO_2 sequestration, J. CO_2 Util. 51 (2021) 101633. http://10.1016/j.jcou.2021.101633
[38] D. Wang, T. Noguchi, T. Nozaki, Increasing efficiency of carbon dioxide sequestration through high temperature carbonation of cement-based materials, Journal of Cleaner Production 238 (2019) 117980. http://10.1016/j.jclepro.2019.117980
[39] P. Liu, Z. Yu, Y. Chen, Carbonation depth model and carbonated acceleration rate of concrete under different environment, Cement and Concrete Composites 114 (2020) 103736. http://10.1016/j.cemconcomp.2020.103736
[40] T. Chen, X. Gao, Effect of carbonation curing regime on strength and microstructure of Portland cement paste, J. CO_2 Util. 34 (2019) 74–86. http://doi.org/10.1016/j.jcou.2019.05.034
[41] X. Xian, D. Zhang, H. Lin, et al., Ambient pressure carbonation curing of reinforced concrete for CO_2 utilization and corrosion resistance, J. CO_2 Util. 56 (2022) 101861. http://10.1016/j.jcou.2021.101861
[42] H. Bao, T. Wang, M. Yu, et al., Experimental study and numerical modeling of supercritical carbonation

of steel fiber reinforced concrete, Construction and Building Materials 476 (2025) 141249. http://10.1016/j.conbuildmat.2025.141249
[43] Q. Liu, A. Cheng, A. Singh, et al., Performance enhancement of recycled concrete through carbonation during ready-mix and curing, Construction and Building Materials 458 (2025) 139665. http://10.1016/j.conbuildmat.2024.139665
[44] B.J. Zhan, D.X. Xuan, C.S. Poon, et al., Effect of curing parameters on CO_2 curing of concrete blocks containing recycled aggregates, Cement and Concrete Composites 71 (2016) 122-130. http://10.1016/j.cemconcomp.2016.05.002
[45] S. Ndiaye, J.-S. Condoret, F. Bourgeois, et al., High-pressure carbonation of mortar as a model for recycled concrete aggregates, The Journal of Supercritical Fluids 198 (2023) 105932. http://10.1016/j.supflu.2023.105932
[46] GB/T 14685-2022, Pebble and crushed stone for construction. 2022-04-15. (in chinese)
[47] D. Sun, W. Huang, K. Liu, et al., Effect of the moisture content of recycled aggregate on the mechanical performance and durability of concrete, Materials 15(18) (2022) 6299. http://10.3390/ma15186299
[48] A. Salas_Montoya, C.-W. Chung, B.E. Mira_Rada, Interaction effect of recycled aggregate type, moisture state, and mixing process on the properties of high-performance concretes, Case Studies in Construction Materials 18 (2023) e02208. http://10.1016/j.cscm.2023.e02208
[49] Y. Wu, Z. Qi, M. Niu, et al., Effect of Moisture Condition of Brick–Concrete Recycled Coarse Aggregate on the Properties of Concrete, Materials 15(20) (2022). http://10.3390/ma15207204
[50] GB/T 25177-2010, Recycled coarse aggregate for concrete. 2010-09-26. (in chinese)
[51] J. Liu, K. Ma, J. Shen, et al., Influence of recycled concrete aggregate enhancement methods on the change of microstructure of ITZs in recycled aggregate concrete, Construction and Building Materials 371 (2023) 130772. http://10.1016/j.conbuildmat.2023.130772
[52] P. Jiang, F. Wang, N. Li, et al., Polyurethane foam lightweight concrete: Preparation, CO_2 fixation properties and mechanism, J. CO_2 Util. 97 (2025) 103109. http://10.1016/j.jcou.2025.103109
[53] B. Graybeal, M. Davis, Cylinder or cube: strength testing of 80 to 200 MPa (11.6 to 29 ksi) ultra-high-performance fiber-reinforced concrete, ACI Materials Journal 105(6) (2008) 603. http://10.14359/20202
[54] S.J.A. Hosseini, A.B.A. Rahman, Effects of spiral confinement to the bond behavior of deformed reinforcement bars subjected to axial tension, Engineering structures 112 (2016) 1-13. http://10.1016/j.engstruct.2015.12.038
[55] GB/T 50080-2016, Standard for test method of performance on ordinary fresh concrete 2016-08-18. (in chinese)
[56] H. Gao, H. Liao, M. Wang, et al., Reinforcing the physicochemical properties of concrete through synergism of CO2 curing and Ca(OH)2 solution drenching, Construction and Building Materials 280 (2021) 122546. http://10.1016/j.conbuildmat.2021.122546
[57] S. Tang, J. Huang, L. Duan, et al., A review on fractal footprint of cement-based materials, Powder Technology 370 (2020) 237-250. http://10.1016/j.powtec.2020.05.065
[58] Y. Yahui, X. Gang, T. Bin, Carbonation characteristics of cement-based materials under the uniform distribution of pore water, Construction and Building Materials 275 (2021) 121450. http://10.1016/j.conbuildmat.2020.121450
[59] S. von Greve-Dierfeld, B. Lothenbach, A. Vollpracht, et al., Understanding the carbonation of concrete with supplementary cementitious materials: a critical review by RILEM TC 281-CCC, Materials and structures 53(6) (2020) 136. http://10.1617/s11527-020-01558-w
[60] H. Bao, R. Wang, Y. Yang, et al., Effect of pore water saturation on the supercritical carbonation of cementitious materials, Materials and Structures 58(6) (2025) 1-22. http://10.1617/s11527-025-02740-8
[61] GB/T 50082-2024, Standard for test methods of long-term performance and durability of concrete. 2024-08-23. (in chinese)
[62] GB/T 50081-2019, Standard for test methods of concrete physical and mechanical properties. 2019-06-19. (in chinese)
[63] J. Lapeyre, S.A. Ponduru, M. Okoronkwo, et al., Hydration of high-alumina calcium aluminate cements with carbonate and sulfate additives, Journal of Thermal Analysis and Calorimetry 147(10) (2021) 5575-5587. http://10.1007/s10973-021-10939-4
[64] N. Russo, F. Lollini, Effect of carbonated recycled coarse aggregates on the mechanical and durability properties of concrete, Journal of Building Engineering 51 (2022). http://10.1016/j.jobe.2022.104290
[65] N. Hosseinzadeh, P. Suraneni, Synergistic effects of air content and supplementary cementitious materials in reducing damage caused by calcium oxychloride formation in concrete, Cement and

827 Concrete Composites 122 (2021) 104170. http://10.1016/j.cemconcomp.2021.104170
828 [66] C. Liang, J. Bao, F. Gu, et al., Determining the importance of recycled aggregate characteristics affecting
829 the elastic modulus of concrete by modeled recycled aggregate concrete: Experiment and numerical
830 simulation, Cement and Concrete Composites 162 (2025) 106118.
831 http://10.1016/j.cemconcomp.2025.106118
832 [67] X. Bao, L. Wang, Y. Ding, et al., Study on the mechanical properties and carbonation of concrete under
833 different phases of CO_2, Journal of Building Engineering 113 (2025) 114150.
834 http://10.1016/j.jobe.2025.114150
835 [68] B. Li, A. Gao, Y. Li, et al., Effect of silica fume content on the mechanical strengths, compressive stress–
836 strain behavior and microstructures of geopolymeric recycled aggregate concrete, Construction and
837 Building Materials 384 (2023) 131417. http://10.1016/j.conbuildmat.2023.131417
838 [69] M. Sumesh, U.J. Alengaram, M.Z. Jumaat, et al., Incorporation of nano-materials in cement composite
839 and geopolymer based paste and mortar – A review, Construction and Building Materials 148 (2017)
840 62-84. http://10.1016/j.conbuildmat.2017.04.206
841 [70] S. Tejas, D. Pasla, Assessment of mechanical and durability properties of composite cement-based
842 recycled aggregate concrete, Construction and Building Materials 387 (2023) 131620.
843 http://10.1016/j.conbuildmat.2023.131620
844 [71] S. Omary, E. Ghorbel, G. Wardeh, Relationships between recycled concrete aggregates characteristics
845 and recycled aggregates concretes properties, Construction and Building Materials 108 (2016) 163-174.
846 http://10.1016/j.conbuildmat.2016.01.042
847 [72] H. Bao, G. Xu, M. Yu, et al., Evolution of ITZ and its effect on the carbonation depth of concrete under
848 supercritical CO_2 condition, Cement and Concrete Composites 126 (2022) 104336.
849 http://10.1016/j.cemconcomp.2021.104336
850 [73] S.N. Abbas, M.I. Qureshi, An investigation of mechanical properties of Self Compacting Concrete (SCC)
851 after addition of Ground Granulated Blast Furnace Slag (GGBFS) and Fly Ash (FA), Materials
852 Chemistry and Physics: Sustainability and Energy 2 (2025) 100008.
853 http://10.1016/j.macse.2025.100008
854 [74] M. Liu, S. Hong, Y. Wang, et al., Compositions and microstructures of hardened cement paste with
855 carbonation curing and further water curing, Construction and Building Materials 267 (2021) 121724.
856 http://10.1016/j.conbuildmat.2020.121724
857 [75] P. He, S. Drissi, X. Hu, et al., Investigation on the influential mechanism of FA and GGBS on the
858 properties of CO_2-cured cement paste, Cement and Concrete Composites 142 (2023) 105186.
859 http://10.1016/j.cemconcomp.2023.105186
860 [76] K.Kobayashi, K.Suzuki, Carbonation of concrete structures and decomposition of C-S-H, Cement and
861 Concrete Resrarch 24 (1993) 55-61. http://10.1016/0008-8846(94)90082-5
862 [77] Y. Ma, W. Li, M. Jin, et al., Influences of leaching on the composition, structure and morphology of
863 calcium silicate hydrate (C–S–H) with different Ca/Si ratios, Journal of Building Engineering 58 (2022)
864 105017. http://10.1016/j.jobe.2022.105017
865 [78] X. Li, Y. Fan, C. Wu, et al., Advances in Molecular Dynamics-Based Characterization of Water and Ion
866 Adsorption and Transport in CSH Gels, Polymers 16(23) (2024) 3285. http://10.3390/polym16233285
867 [79] X.M. Aretxabaleta, J. López-Zorrilla, I. Etxebarria, et al., Multi-step nucleation pathway of CSH during
868 cement hydration from atomistic simulations, Nature Communications 14(1) (2023) 7979.
869 http://10.1038/s41467-023-43500-y
870 [80] A. Cuesta, I. Santacruz, G. Angeles, et al., Local structure and Ca/Si ratio in CSH gels from hydration
871 of blends of tricalcium silicate and silica fume, Cement and Concrete Research 143 (2021) 106405.
872 http://10.1016/j.cemconres.2021.106405
873 [81] Y. Zhu, Q. Zhu, F. Qi, Research Progress on the Preparation and Comprehensive Utilization of Calcium
874 Silicate Hydrate from Solid Waste, Bulletin of the Chinese Ceramic Society 43(2) (2024). (in chinese)
875 http://10.16552/j.cnki.issn1001-1625.2024.02.022
876 [82] R. Mi, T. Yu, C.S. Poon, Feasibility of utilising porous aggregates for carbon sequestration in concrete,
877 Environmental Research 228 (2023) 115924. http://10.1016/j.envres.2023.115924
878 [83] D. Fan, J.-X. Lu, X.-S. Lv, et al., Carbon capture and storage CO_2 foam concrete towards higher
879 performance: Design, preparation and characteristics, Cement and Concrete Composites 157 (2025)
880 105925. http://10.1016/j.cemconcomp.2025.105925
881 [84] A. Dixit, H. Du, S.D. Pang, Carbon capture in ultra-high performance concrete using pressurized CO_2
882 curing, Construction and Building Materials 288 (2021) 123076.
883 http://10.1016/j.conbuildmat.2021.123076

[85] Q. Liu, Y. Wang, C. Sun, et al., Carbon sequestration and mechanical properties of foam concrete based on red mud pre-carbonation and CO_2 foam bubbles, Construction and Building Materials 426 (2024) 135961. http://10.1016/j.conbuildmat.2024.135961
[86] X. Zhang, S. Liu, G. Cai, et al., Scaled model test into the spatial variability and carbon storage potential of carbon sequestration foamed concrete as a subgrade filler, Construction and Building Materials 471 (2025) 140718. http://10.1016/j.conbuildmat.2025.140718
[87] J. Liu, G. Liu, W. Zhang, et al., A new approach to CO_2 capture and sequestration: A novel carbon capture artificial aggregates made from biochar and municipal waste incineration bottom ash, Construction and Building Materials 398 (2023) 132472. http://10.1016/j.conbuildmat.2023.132472
[88] X. Chen, S. Li, M. Hu, et al., Early age accelerated carbonation of cementitious materials surface in low CO_2 concentration condition, Construction and Building Materials 445 (2024). http://10.1016/j.conbuildmat.2024.137975
[89] Y. Jiang, Z. Ma, Y. Gao, et al., A review on the impact of water in accelerated carbonation: Implications for producing sustainable construction materials, Cement and Concrete Composites 157 (2025). http://10.1016/j.cemconcomp.2024.105902